

Estimates of Gradients in Radar Moments Using a Linear Least Squares Derivative Technique

MATTHEW C. MAHALIK, BRANDON R. SMITH, KIMBERLY L. ELMORE, DARREL M. KINGFIELD,^a
KIEL L. ORTEGA, AND TRAVIS M. SMITH

Cooperative Institute for Mesoscale Meteorological Studies, University of Oklahoma, and NOAA/OAR National Severe Storms Laboratory, Norman, Oklahoma

(Manuscript received 6 June 2018, in final form 27 January 2019)

ABSTRACT

The local, linear, least squares derivative (LLSD) approach to radar analysis is a method of quantifying gradients in radar data by fitting a least squares plane to a neighborhood of range bins and finding its slope. When applied to radial velocity fields, for example, LLSD yields part of the azimuthal (rotational) and radial (divergent) components of horizontal shear, which, under certain geometric assumptions, estimate one-half of the two-dimensional vertical vorticity and horizontal divergence equations, respectively. Recent advances in computational capacity as well as increased usage of LLSD products by the meteorological community have motivated an overhaul of the LLSD methodology's application to radar data. This paper documents the mathematical foundation of the updated LLSD approach, including a complete derivation of its equation set, discussion of its limitations, and considerations for other types of implementation. In addition, updated azimuthal shear calculations are validated against theoretical vorticity using simulated circulations. Applications to nontraditional radar data and new applications to nonvelocity radar data including reflectivity at horizontal polarization, spectrum width, and polarimetric moments are also explored. These LLSD gradient calculations may be leveraged to identify and interrogate a wide variety of severe weather phenomena, either directly by operational forecasters or indirectly as part of future automated algorithms.

1. Introduction

Weather radars are crucial to identifying and understanding weather phenomena. Signatures of precipitation type and rate, airmass boundaries, and storm rotation are often identifiable by the size, shape, and location of gradients within specific radar fields. In reflectivity at horizontal polarization Z_H alone, the hook echo of a supercell (Fujita 1973; Markowski 2002), a bow-shaped Z_H maximum common to damaging wind events (Przybylinski 1995), and the manifestation of tornadic debris in the form of a “debris ball” (Burgess et al. 2002) can all be thought of as gradients. Likewise, gradient patterns such as differential reflectivity Z_{DR} arcs (Kumjian and Ryzhkov

2008) and tornado debris signatures (TDS; Ryzhkov et al. 2005) within polarimetric data fields such as Z_{DR} and cross-correlation coefficient ρ_{hv} aid in the detection and tracking of tornadoes and diagnostics of updraft characteristics.

Radial velocity V_r gradients have been the subject of perhaps the most study with respect to severe storms. Among a wide range of applications, V_r gradients are used to help identify convergence along boundaries, which may be either the result of or catalyst for convection (Carbone et al. 1990; Wilson et al. 1992), midlevel convergence within a thunderstorm that can signal the onset of damaging winds (Schmocker et al. 1996), divergent flows from downdrafts impinging on the surface or storm exhaust at the cloud top (Roberts and Wilson 1989; Smith et al. 2004), and rotation associated with mesocyclones (Donaldson 1970) and tornadoes (Donaldson 1978; Brown et al. 1978). More recently, relationships between the magnitudes of V_r gradients in rotation signatures (measured as velocity difference, rotational velocity, etc.) and tornado occurrence, intensity, and damage probability, have been

^a Current affiliation: Cooperative Institute for Research in Environmental Sciences, University of Colorado, and NOAA/OAR/ESRL/Global Systems Division, Boulder, Colorado.

Corresponding author: Matthew Mahalik, matthew.mahalik@noaa.gov

derived (Alexander and Wurman 2008; Smith et al. 2015; Thompson et al. 2017).

Typically, the relative magnitude of rotation in severe local storms is quantified as the magnitude of the difference between the local maxima in inbound and outbound V_r . This “peak-to-peak” technique yields a quantity often referred to as “delta velocity,” which may be normalized by the distance between the V_r extrema (Mitchell et al. 1998; Stumpf et al. 1998). This one-dimensional approach is effective in estimating the relative, local rate of rotation, but it excludes surrounding data points, which may include valuable information about the rotating feature beyond simply the maximum rotation rate at its core. Other limiting assumptions of the peak-to-peak approach include the following: 1) the center of the circulation lies exactly between the extrema, which may not be possible to determine with coarse beamwidths and physical radar sampling limitations (Burgess et al. 1993; Wood and Brown 1997); 2) the extrema themselves are accurate measurements, which is not always true due to noisy or poorly dealiased data (Zittel et al. 2001); and 3) peak-to-peak delta velocity will usually be biased low unless the tornado is very wide, due to azimuthal smearing and averaging of the radar beam over a relatively narrow wind max (Wood and Brown 2011).

In response to the need for an alternative approach to quantifying V_r gradients in a mathematically robust but sufficiently straightforward way for real-time computation and operational use, Elmore et al. (1994) and Smith and Elmore (2004, hereafter SE04) introduced the linear, least squares derivative (LLSD) approach to radar data analysis. LLSD is a statistical data analysis approach that quantifies the gradient of a scalar field as a two-dimensional, least squares plane that is fit to a local neighborhood (or “kernel”) of V_r data or other radar measurements. The slope of this best-fit plane is the local gradient at the center of the kernel. This approach includes local information about the entire feature by using surrounding data and effectively smoothing extreme values to minimize the effect of outliers caused by poor data quality. The total gradient is decomposed into azimuthal and radial components, which are calculated simultaneously for any given radar scan. When applied to V_r fields, the across-azimuth gradient represents the rotational shear component, referred to as “AzShear” (azimuthal shear; Miller et al. 2013). The complementary, along-azimuth V_r gradient yields the divergent shear component, or “DivShear.” Typical AzShear and DivShear fields for a tornadic supercell are shown in Fig. 1.

Although V_r is a vector directed along the radial, treating it as a local scalar provides numerous advantages. For example, scalar LLSD gradients can be easily gridded for research or operational use. At the time of

this writing, gridded AzShear is an operational product within the Multi-Radar Multi-Sensor (MRMS) system (Smith et al. 2016). In recent years, the application of AzShear in a wide range of operational and research initiatives (Heinselman et al. 2008, 2012; Stumpf et al. 2012; Davis and Parker 2014; Snyder and Ryzhkov 2015; Skinner et al. 2016; Dawson et al. 2017; Stough et al. 2017, among others), coupled with an increase in computational capacity, has motivated attempts to improve the accuracy of LLSD-derived products. For example, Miller et al. (2013) and Newman et al. (2013) described postprocessing methods to overcome general limitations of the LLSD technique by improving the ability of AzShear to identify rotation at the storm and tornado scales through the use of multiple hypothesis tracking (a technique used to isolate continuous tracks of rotating objects) and empirically derived, range-based shear corrections, respectively.

Unlike postprocessing approaches, the work presented here focuses directly on the underlying LLSD equations and specific improvements upon the original SE04 methodology and provides a technique generalized for calculating LLSD gradients of any data field. The LLSD equations were rederived without regard to the simplifying assumptions discussed in SE04, which were at the time necessitated by computational limitations. Updated LLSD outputs of AzShear were then validated using a suite of simulated Rankine vortices with known rotation attributes (size, strength, and range from radar). In addition, the LLSD equations were applied to a variety of radar fields to investigate the method’s utility in a range of meteorological phenomena, producing gradient fields beyond only AzShear for both V_r and non- V_r radar variables.

The effectiveness of direct use of LLSD gradients by forecasters is dependent on the application. For example, while time-accumulated AzShear (often referred to as “rotation tracks”; Miller et al. 2013) has been demonstrated as a valuable tool for relaying tornado information to end users (Kuster et al. 2017), gradient fields of ρ_{hv} may be less intuitive. In essence, all LLSD gradients are quantitative representations of signatures that human forecasters are trained to visually identify but that can sometimes be difficult to quantify. As a result, many of the examples presented here show more promise as an intermediate product toward future feature-identification or interrogation algorithm development.

In this paper, the mathematical derivation of the complete set of LLSD equations is shown in section 2. Section 3 discusses the mathematic and geometric considerations of the LLSD kernel, and section 4 provides examples of LLSD applications to various radar data. The LLSD fields shown throughout were produced using the National Severe Storms Laboratory (NSSL)

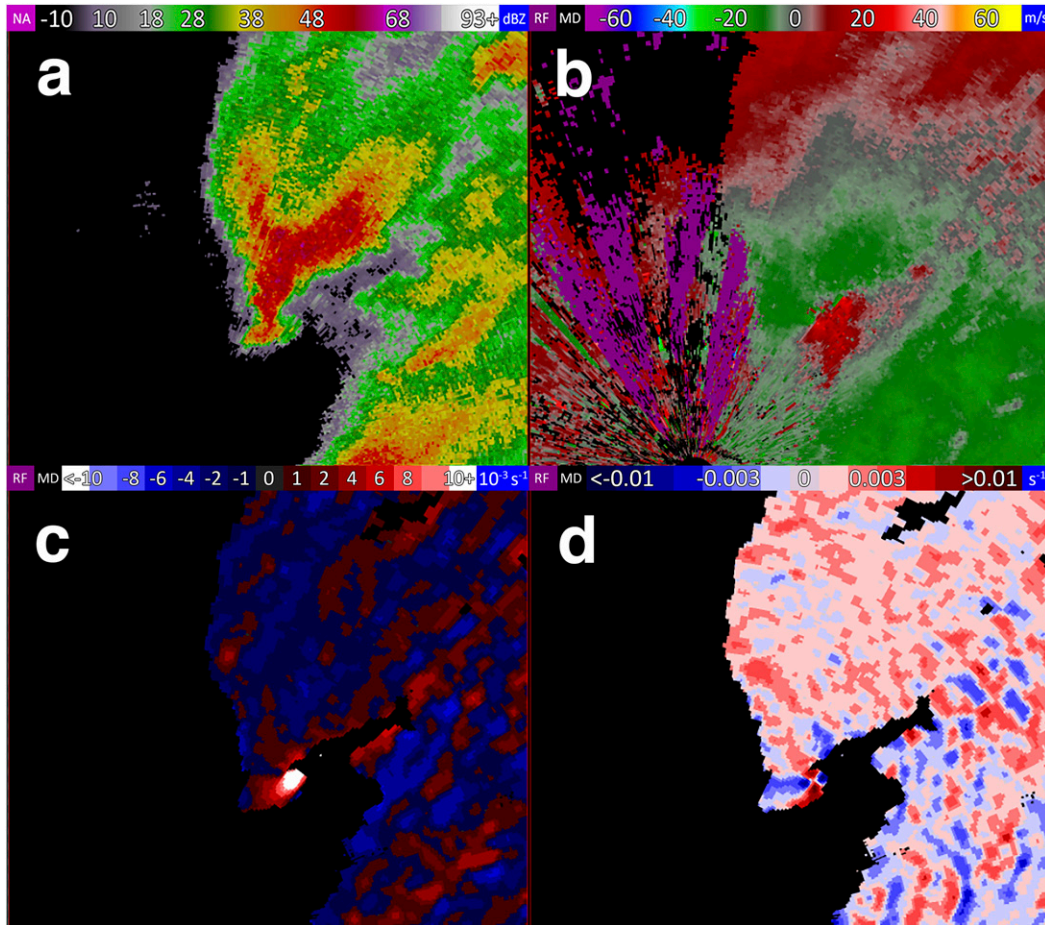


FIG. 1. Single-radar (a) 0.5° QC Z_H , (b) 0.5° dealiased V_r , (c) 0.5° AzShear, and (d) 0.5° DivShear depiction of a tornadic supercell from the Cheyenne, WY (KCYS), radar at 2231 UTC 12 Jun 2017. The low-level mesocyclone is visible in (c) as a maximum in AzShear (white) and in (d) as coupled extrema of positive and negative DivShear (deep red and blue, respectively). AzShear and DivShear are thresholded by >20 dBZ 0.5° QC Z_H .

Warning Decision Support System-Integrated Information (WDSS-II; Lakshmanan et al. 2007b) software suite. Many of the LLSD gradient fields are thresholded by quality-controlled (QC) Z_H (Lakshmanan et al. 2007a) to focus solely on storm processes.

2. Derivation

Before LLSD gradients are calculated for any input field, the data are passed through a median filter (Huang et al. 1979) to reduce noise, fill in potential missing data, and filter outliers. Any input V_r data should be dealiased beforehand. The filter used by NSSL LLSD algorithms measures three azimuths across by three range gates deep and assigns the median value of those nine data points to the center gate of the neighborhood if at least five of the eight surrounding gates contain valid data. Measurements within the 3×3 neighborhood are assumed to occur at regular radius and azimuth intervals.

This filter is applied to each individual data point within the field. Any gates with missing or range-folded data remaining in its kernel are discarded. The resulting filtered data are then passed to the LLSD equations.

The original LLSD equations introduced by Elmore et al. (1994) and expanded by SE04 were simplified at the time for computational efficiency. In particular, it was assumed that the data within the LLSD kernel are locally Cartesian and symmetric about the kernel center. As such, these calculations implemented a locally constant azimuthal spacing between data points. This assumption becomes especially problematic in two situations. First, near the radar, the inclusion of additional, azimuthally narrow gates may cause the LLSD kernel to wrap around the radar such that the straight-line distance across the kernel may be smaller than the polar-coordinate distance within the kernel. As a result, the gradient would be calculated across a smaller distance, producing artificially high shears surrounding the

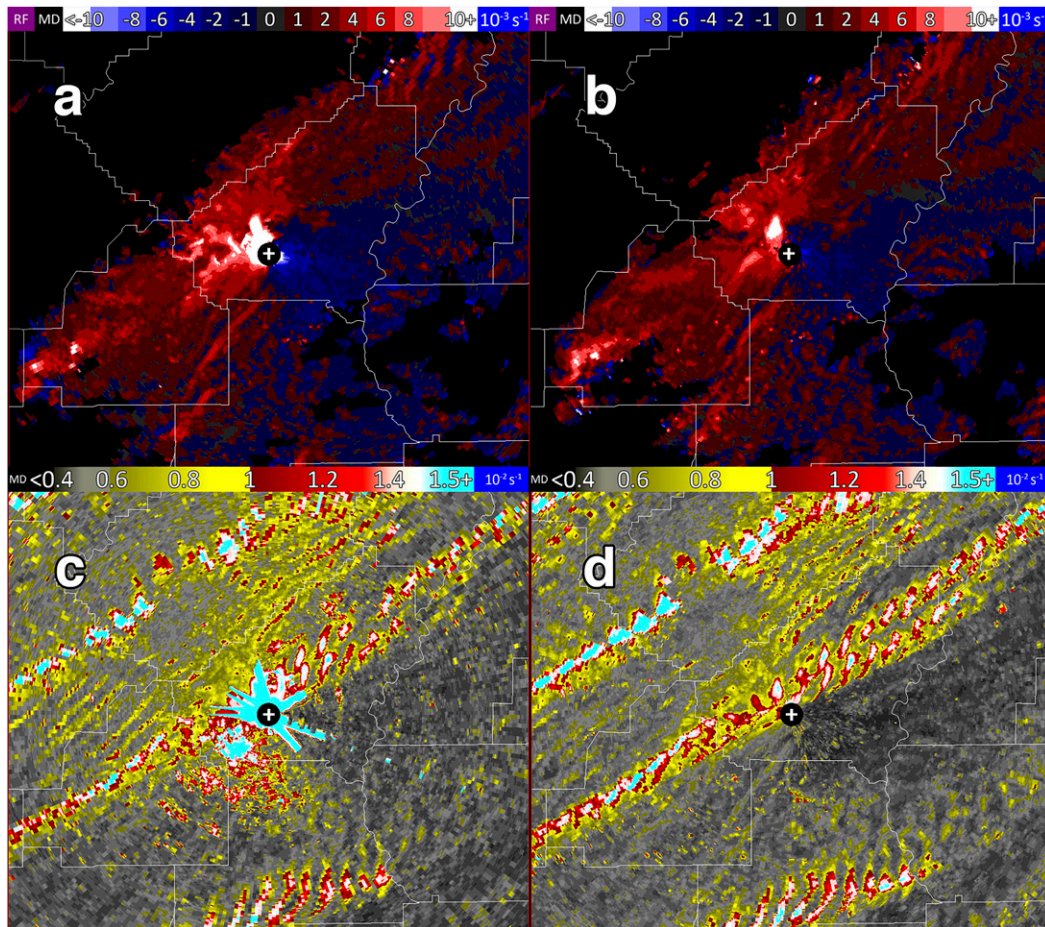


FIG. 2. Single-radar 0–2 km AGL layer-maximum AzShear for a tornadic supercell near the Birmingham, AL (KBMX), radar (denoted by the white cross) at 0009 UTC 28 Apr 2011 calculated using (a) legacy LLS equations and (b) the updated LLS algorithm, and single-radar 0–2 km AGL rotation tracks for the 12-h period ending 0300 UTC 28 Apr 2011 using (c) legacy and (d) updated LLS equations. The vortex path is more easily identifiable in both the instantaneous AzShear and accumulated tracks using the updated LLS algorithm in (b) and (d), where artificially high AzShear is not present.

radar location. Second, if the LLS kernel covers a large distance radially (as in along-radial gradient applications), the Cartesian assumption may be violated because the radar beam physically broadens with range, also decreasing the across-beam resolution with distance from the radar. If the change in azimuthal spacing is sufficiently large, the gradient would be calculated over a larger horizontal distance, resulting in artificially low AzShear.

Given recent increases in processing capabilities, an updated LLS methodology was developed from the full derivation below, which is not subject to the same restrictions. While the updated equations greatly alleviate these problems (section 3), the method is not perfect at very large or small distances from the radar due to sampling limitations, and similar but less-severe artifacts may be present in some situations.

Since LLS calculates a best-fit plane for areas across several data points, we use a general, linear, least squares approximation, which yields the largest rate of change in any direction. This estimate is derived from the minimization of a general, first-order, planar equation as in Eq. (1):

$$\mu(b, c) = a_0 + a_1(b) + a_2(c), \quad (1)$$

where $\mu(b, c)$ is the linear fit of the coefficient vector $\mathbf{u} = [a_0 \ a_1 \ a_2]$, modified by coefficients b and c . For meteorological purposes, the three components of \mathbf{u} include a constant u_0 , and the radial u_r and azimuthal u_θ derivatives (shears) of a field [Eq. (2)]:

$$\mathbf{u} = [u_0 \ u_r \ u_\theta]. \quad (2)$$

This shear vector can be found by minimizing the sum of squares over n data points. This sum of squares R

may be locally weighted by weight w_i , within the LLS kernel [Eq. (3)]:

$$R \equiv \sum_{i=1}^n w_i [Y_i - \mu(b, c)]^2. \quad (3)$$

The linear fit is a function of the response variable Y_i . For radar data, Y_i is a two-dimensional radar variable u_{ij} , which is itself dependent on the offset, in range Δr_{ij} and azimuth $\Delta \theta_{ij}$, from the kernel center ($r = 0, \theta = 0$), where $\Delta \theta_{ij}$ (Δr_{ij}) is a distance in the azimuthal (radial) direction. If we define the kernel dimensions as $m \times n$ such that index i (j) runs from $i = 0$ to $i = m$ (from $j = 0$ to $j = n$), then R can be calculated over each point $k = (i, j)$ within the kernel. A discussion of kernel size considerations is presented in section 3. Then, μ [Eq. (1)] and R [Eq. (3)] can be reformulated as Eqs. (4) and (5):

$$\mu(r, \theta) = u(r, \theta) = u_0 + u_r \Delta r_k + u_\theta \Delta \theta_k, \quad \text{and} \quad (4)$$

$$R = \sum_{k=0}^{m \times n} w_k [u(r_k, \Delta \theta_k) - (u_0 + u_r \Delta r_k + u_\theta \Delta \theta_k)]^2. \quad (5)$$

As dictated by the least squares technique, R is minimized by setting its derivative to zero in each direction. This yields the following normal, linear, least squares derivatives [Eqs. (6a)–(6c)]:

$$\frac{\partial R}{\partial u_r} = 0 = \sum_{k=0}^{m \times n} 2(-u_k + u_0 + u_r \Delta r_k + u_\theta \Delta \theta_k) w_k \Delta r_k, \quad (6a)$$

$$\frac{\partial R}{\partial u_\theta} = 0 = \sum_{k=0}^{m \times n} 2(-u_k + u_0 + u_r \Delta r_k + u_\theta \Delta \theta_k) w_k \Delta \theta_k, \quad \text{and} \quad (6b)$$

$$\frac{\partial R}{\partial u_0} = 0 = \sum_{k=0}^{m \times n} 2(-u_k + u_0 + u_r \Delta r_k + u_\theta \Delta \theta_k) w_k. \quad (6c)$$

Terms in these equations are combined and rearranged to produce the complete system of least squares derivatives [Eqs. (7a)–(7c)]:

$$\begin{aligned} \sum_{k=0}^{m \times n} u_k w_k \Delta r_k &= \sum_{k=0}^{m \times n} u_0 w_k \Delta r_k + \sum_{k=0}^{m \times n} u_r w_k (\Delta r_k)^2 \\ &+ \sum_{k=0}^{m \times n} u_\theta w_k \Delta r_k \Delta \theta_k, \end{aligned} \quad (7a)$$

$$\begin{aligned} \sum_{k=0}^{m \times n} u_k w_k \Delta \theta_k &= \sum_{k=0}^{m \times n} u_0 w_k \Delta \theta_k + \sum_{k=0}^{m \times n} u_r w_k \Delta r_k \Delta \theta_k \\ &+ \sum_{k=0}^{m \times n} u_\theta w_k (\Delta \theta_k)^2, \quad \text{and} \end{aligned} \quad (7b)$$

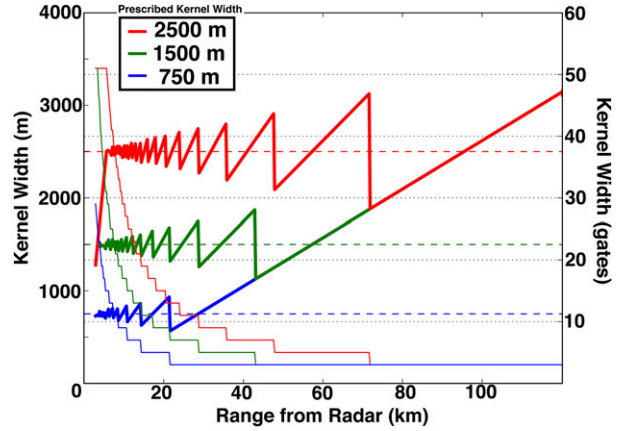


FIG. 3. Summary of the variability of LLS kernel size with range for prescribed azimuthal widths of 750 (blue), 1500 (green), and 2500 m (red) for 0.5° superresolution radar data from a WSR-88D. The actual width of the kernel (m) is shown as the thick line, while the thin lines show the respective number of gates in the kernel. The prescribed kernel widths (m) are provided for reference as horizontal dashed lines. Values for any kernel size converge at some range; here, all three prescribed kernel sizes result in the same true kernel size beyond a range of approximately 72 km.

$$\begin{aligned} \sum_{k=0}^{m \times n} u_k w_k &= \sum_{k=0}^{m \times n} u_0 w_k + \sum_{k=0}^{m \times n} u_r w_k \Delta r_k \\ &+ \sum_{k=0}^{m \times n} u_\theta w_k \Delta \theta_k. \end{aligned} \quad (7c)$$

Here the derivations deviate from SE04, which assumed perfectly symmetrical data about the kernel center and neglected all terms containing off-diagonal coefficients. In this derivation, all terms are preserved.

From Eqs. (7a)–(7c), the individual shear components in Eq. (4) can be found. Equations (7a)–(7c) can be expressed in matrix form as $\mathbf{M}\mathbf{X} = \mathbf{Y}$, where \mathbf{M} is a matrix of the position (Δr_k and $\Delta \theta_k$) and weighting (w_k) coefficients, and \mathbf{X} is a matrix of shear components [Eq. (8)], where all summations remain from $k = 0$ to $k = m \times n$:

$$\begin{aligned} \begin{bmatrix} \sum w_k \Delta r_k \Delta \theta_k & \sum w_k \Delta \theta_k^2 & \sum w_k \Delta \theta_k \\ \sum w_k \Delta r_k^2 & \sum w_k \Delta r_k \Delta \theta_k & \sum w_k \Delta r_k \\ \sum w_k \Delta r_k & \sum w_k \Delta \theta_k & \sum w_k \end{bmatrix} \begin{bmatrix} u_\theta \\ u_r \\ u_0 \end{bmatrix} \\ = \begin{bmatrix} \sum w_k \Delta r_k u_k \\ \sum w_k \Delta \theta_k u_k \\ \sum w_k u_k \end{bmatrix}. \end{aligned} \quad (8)$$

The individual derivatives are found by multiplying the equation by the inverse of the coefficient matrix [Eq. (9)]:

$$\mathbf{X} = \mathbf{M}^{-1}\mathbf{Y}. \quad (9)$$

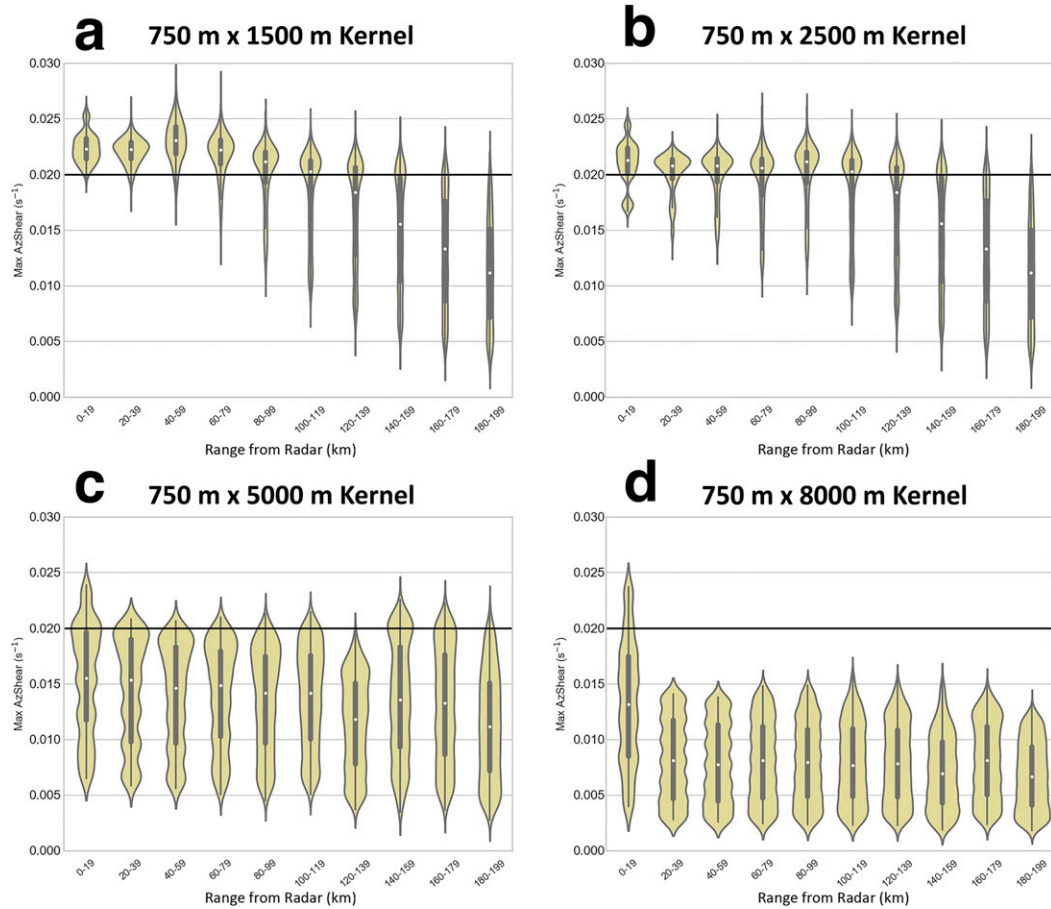


FIG. 4. Violin plots showing the distribution of maximum AzShear values for a suite of vortices simulated by a Rankine combined vortex model with theoretical half- $\zeta = 0.02 \text{ s}^{-1}$ for LLS kernels with target azimuthal widths of (a) 1500, (b) 2500, (c) 5000, and (d) 8000 m.

The inverse of matrix \mathbf{M} can be calculated using the determinant D and adjugate of matrix \mathbf{M} [$\text{adj}(\mathbf{M})$] under the condition $D \neq 0$ [Eq. (10)]. The individual terms of the adjugate matrix are written as a_{ij} :

$$\mathbf{M}^{-1} = \frac{1}{D} \text{adj}(\mathbf{M}) = \begin{bmatrix} a_{11} & a_{12} & a_{13} \\ a_{21} & a_{22} & a_{32} \\ a_{31} & a_{23} & a_{33} \end{bmatrix} \begin{pmatrix} 1 \\ D \end{pmatrix}. \quad (10)$$

This allows Eq. (9) to be expressed as Eq. (11), which can then be solved for both shear components, yielding the final LLS horizontal shear equations for the azimuthal [Eq. (12a)] and divergent [Eq. (12b)] components:

$$\begin{bmatrix} u_{\theta} \\ u_r \\ u_0 \end{bmatrix} = \begin{bmatrix} a_{11}/D & a_{12}/D & a_{13}/D \\ a_{21}/D & a_{22}/D & a_{32}/D \\ a_{31}/D & a_{23}/D & a_{33}/D \end{bmatrix} \begin{bmatrix} \sum w_k \Delta r_k u_k \\ \sum w_k \Delta \theta_k u_k \\ \sum w_k u_k \end{bmatrix}, \quad (11)$$

$$u_{\theta} = \sum_{k=0}^{m \times n} w_k \Delta r_k u_k \left(\frac{a_{11}}{D} \right) + \sum_{k=0}^{m \times n} w_k \Delta \theta_k u_k \left(\frac{a_{12}}{D} \right) + \sum_{k=0}^{m \times n} w_k u_k \left(\frac{a_{13}}{D} \right), \quad \text{and} \quad (12a)$$

$$u_r = \sum_{k=0}^{m \times n} w_k \Delta r_k u_k \left(\frac{a_{21}}{D} \right) + \sum_{k=0}^{m \times n} w_k \Delta \theta_k u_k \left(\frac{a_{22}}{D} \right) + \sum_{k=0}^{m \times n} w_k u_k \left(\frac{a_{23}}{D} \right). \quad (12b)$$

The fully expanded forms of Eqs. (12a) and (12b) and list of variables for each are found in [appendixes A and B](#), respectively. Some of the variables in these equations can be adjusted to suit specific research needs. Several of the aspects discussed in [section 3](#) are in the context of the current, operational MRMS configuration, though all are important considerations for any application of the LLS technique.

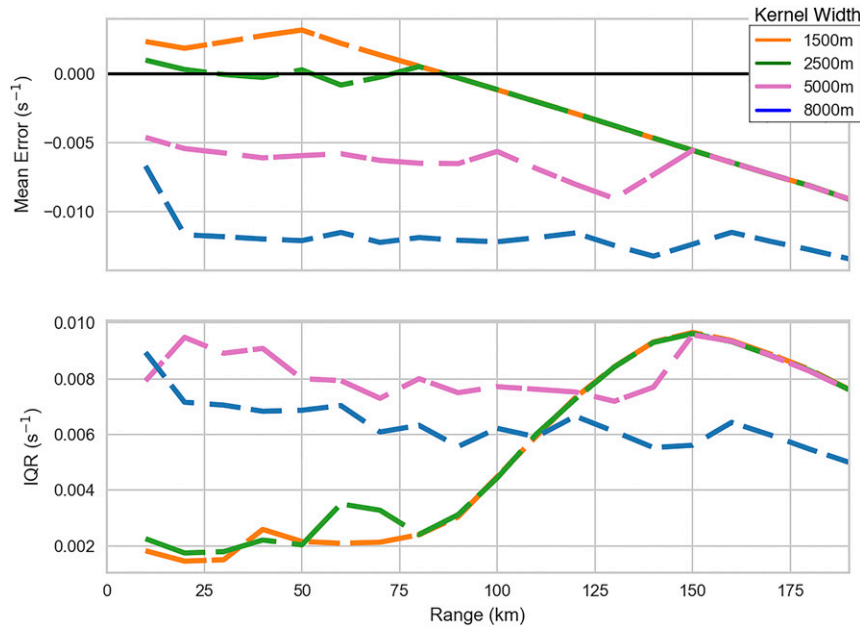


FIG. 5. (top) Average error (calculated as the mean of all differences between calculated AzShear and theoretical AzShear) and (bottom) average median-centered IQR (the difference between the 75th and 25th percentile values) of all simulated vortices in Fig. 4 with theoretical half- $\zeta = 0.02 \text{ s}^{-1}$ for LLSD kernels with target azimuthal widths of 1500, 2500, 5000 m, and 8000 m. At range < 100 km, smaller kernels tend to have lower mean errors and lower IQR, suggesting more consistency and accuracy, and less sensitivity to circulation geometry.

3. Discussion

Much of the immediate utility of the LLSD equation adjustments can be seen in two-dimensional gradient fields of radar data, as in Figs. 1c and 1d. LLSD gradients are calculated for and assigned to each individual gate occupied by valid input radar data. They are pieced together onto the same grid as the input field, resulting in complete gradient fields that are used to visualize gradients within the context of an entire radar scan. Internal testing of LLSD-derived products has shown an improvement of AzShear and other LLSD gradient calculations using the updated LLSD equations over legacy equations. For example, much of the artificially high AzShear within 5–10 km of the radar, commonly observed with legacy LLSD equations, is mitigated using the updated LLSD algorithm, allowing vortices very near the radar to be more easily distinguished (Fig. 2).

a. Kernel size considerations

All LLSD gradient calculations are highly sensitive to the size of the LLSD kernel. For example, consider the AzShear calculation for a hypothetical, symmetrical, isolated vortex in the center of the kernel. Assuming the entire vortex fits within the kernel, a large kernel will include more low-shear gates away from the vortex core

than a smaller one, thereby reducing the overall shear within the kernel. Conversely, a small kernel is susceptible to missing gates that lie on the outer edge of a circulation, thus slightly overestimating the maximum rotation of the vortex as a whole.

The LLSD algorithm uses a constant, predefined kernel size (in meters). It may be manually adjusted to best suit the type of analysis being performed but is constant across the volume during processing. For example, AzShear uses a kernel with a prescribed azimuthal width of 2500 m and radial depth of 750 m, and DivShear uses kernel dimensions of 750-m azimuthal width by 1500-m radial depth. In general, the azimuthal dimension of a kernel used to calculate across-azimuth gradients should be at least as large as its radial dimension, and vice versa.

Because of the physical limitations of radar sampling, azimuthal spacing increases with range. To maintain an approximately constant physical kernel width, the number of azimuthal gates within the kernel decreases with range to compensate for increasing gate widths. Thus, at small ranges from the radar, the kernel contains a greater number of radials than a kernel located at a larger range. At each range, the number of radials required to construct the kernel is explicitly calculated, meaning that the kernel size updates as frequently as geometrically possible to maintain an accurate width. This adaptive

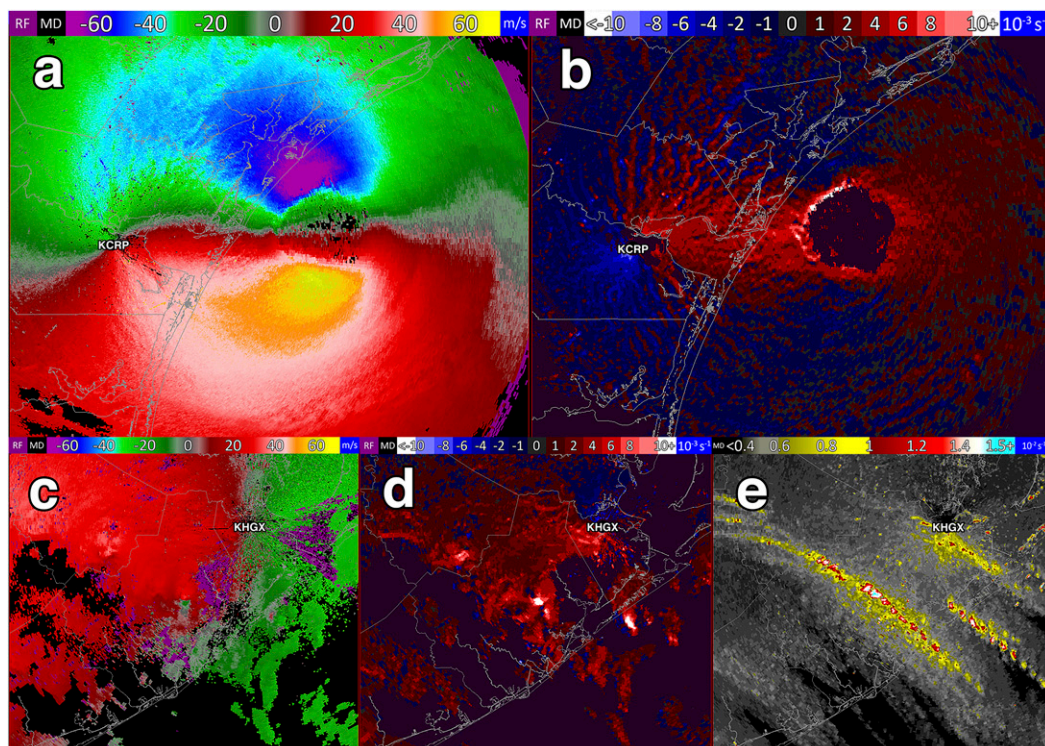


FIG. 6. Single-radar observations during Hurricane Harvey on 26 Aug 2017: (a) 0.5° dealiased V_r , and (b) corresponding 0–2 km AGL layer-maximum AzShear from the Corpus Christi, TX (KCRP), radar near the center of Hurricane Harvey at 0039 UTC, shortly before landfall; (c) dealiased 0.5° velocity associated with outer rainband cells from the Houston/Galveston, TX (KHGX), radar at 0244 UTC, (d) corresponding 0–2 km AGL layer-maximum AzShear, and (e) 2-h accumulated 0–2 km AGL layer-maximum rotation tracks ending at 0252 UTC. In (b), AzShear highlights the strong gradient between major hurricane-force winds in the eyewall and weak winds in the eye. Low-level circulations, some tornadic, are tracked using AzShear in (d) and (e). The AzShear fields were calculated using the same default LLS kernel size.

approach is not perfect and results in 1) inaccuracies at very large or very small distances from the radar and 2) discontinuities at certain ranges in between (Fig. 3). Near the radar, where azimuthal spacing is smallest, the kernel may wrap sufficiently around the radar to violate the assumption that the kernel columns are practically parallel. As a result, an upper limit on the number of radials in a single kernel is imposed. When applying a kernel with an azimuthal width of 2500 m to a 0.5° elevation scan of super-resolution WSR-88D radar data, this limit is 51 radials. This threshold was selected through subjective evaluation of the AzShear product and affects kernels centered at a range of 6 km or less.

The LLS equations mathematically require a minimum of three radials and three range gates within a kernel to calculate the 2D gradient. As the kernel expands laterally with increasing azimuthal spacing, the number of radials that fit inside the kernel will eventually reach this minimum. The range at which this occurs is dependent on radar properties and the prescribed kernel size. At all ranges beyond this point, the

prescribed kernel width is no longer maintained. For an AzShear kernel with an azimuthal width of 2500 m applied to a WSR-88D 0.5° elevation scan, this occurs at ranges greater than approximately 72 km. Beyond this range, the kernel width exceeds the prescribed width, meaning that the derivatives are taken over a larger area, creating a generally lower gradient estimate (Newman et al. 2013). This is visually manifested as a “smearing” effect across radials at large ranges, which is a common artifact of radar data. The default DivShear configuration’s kernel, which is narrower in azimuth, is subject to the same effect, though the smearing problem begins closer to the radar than with AzShear.

b. Kernel weighting

By default, LLS products use a uniform weight for each gate within the kernel, such that $w_k = 1$ for all k in Eqs. (12a) and (12b) (Miller et al. 2013). Another option is to employ a nonuniform weighting scheme, such as Cressman weighting (Cressman 1959), so that gates farther from the center of the kernel receive less weight.

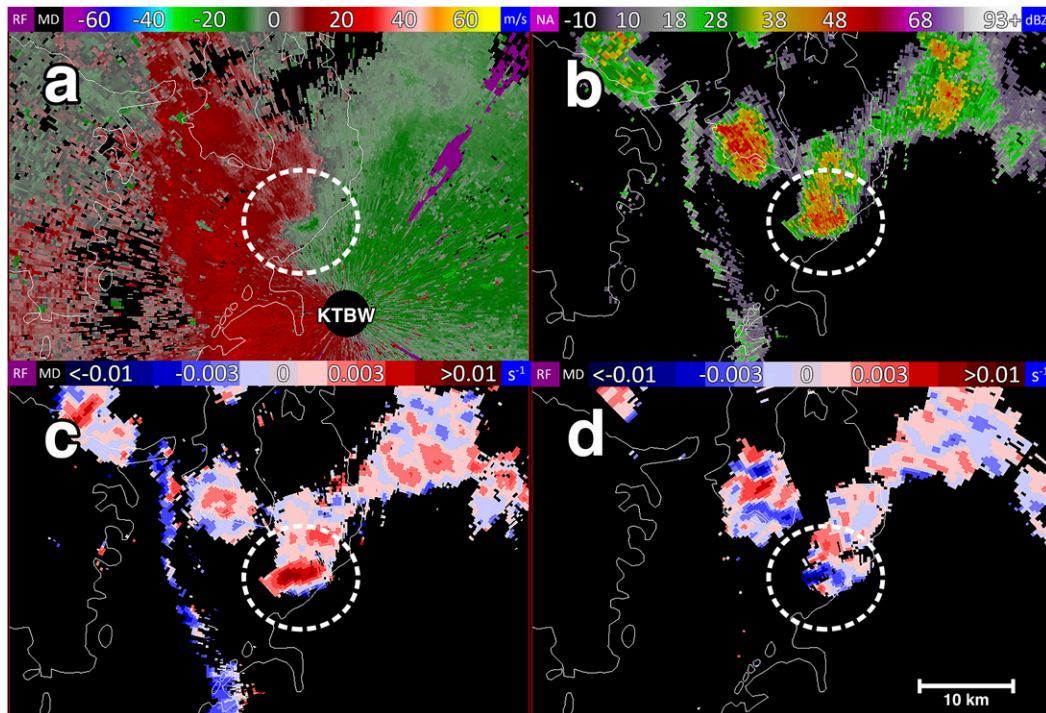


FIG. 7. Single-radar, 0.5° (a) dealiased V_r , (b) QC Z_H , and (c) DivShear, and (d) 10.0° DivShear showing the low-level divergence and midlevel convergence associated with a downburst (denoted by the dashed circle) sampled by the Tampa Bay, FL (KTBW), radar at 2219 UTC 24 Aug 2011. The DivShear in (c) and (d) are thresholded by >10 dBZ 0.5° QC Z_H .

In general, a nonuniform weighting scheme will reduce the magnitudes of the derivatives, except when the kernel is centered on the underlying radar signature (e.g., a mesocyclone), where it will receive near-full weighting. Practically, nonuniform weighting results in increased isolation of features within the input field, which in turn increases gradients within the derivative fields. Internal testing (not shown) of kernel weighting revealed the output derivative fields more quickly yield background-level values as input field features are increasingly offset from the kernel center. Specific radar applications using the LLSA technique should explore the use of weighting schemes as part of their implementation.

c. Validation

Mathematically, when applied to a V_r field, the slope of the LLSA best-fit plane across azimuth θ [Eq. (12a)] is represented as a simple rise over run $\delta V_r / \delta \theta$, which corresponds to one term of ζ , assuming local symmetry. Thus, AzShear can be considered an approximation for one-half of the total ζ . To evaluate this relationship and quantify the effects of kernel size on AzShear, calculations of AzShear were compared to theoretical half- ζ , defined as $\Delta V_r / 2r$ for a variety of simulated circulations. The V_r signatures of simulated vortices of varying size, intensity, and range from a hypothetical WSR-88D

superresolution radar (0.5° azimuthal resolution and 1.02° effective beamwidth) were generated using a Rankine combined vortex model (Wood and Brown 1997). Circulations were varied in radius (1000–8000 m in increments of 250 m), distance to radar (10–200 km in increments of 5 km), and circulation strength ($\Delta V = V_{\max} - V_{\min}$, from 10 to 50 m s^{-1} in increments of 5 m s^{-1}). A total of 10 179 vortices were simulated. Following the approach of SE04 and Miller et al. (2013), 2 m s^{-1} uniform noise was superimposed on the V_r field of each to better simulate the imperfections present in real radar fields.

Each simulated vortex was passed through the LLSA algorithm to calculate AzShear using four different kernels, each with a constant radial depth of 750 m (since a radar's radial resolution should not change) but with different azimuthal widths: 1500, 2500, 5000, and 8000 m. Maximum AzShear calculations for all circulations with theoretical half- ζ of 0.02 s^{-1} , a common value for strongly rotating storms (Burgess et al. 1975), are summarized in Fig. 4. In general for the circulations within 90 km from the radar, a kernel 2500 m wide by 750 m deep produced the most accurate AzShear calculation, with the average maximum AzShear values varying from the theoretical shear by 5% or less (Fig. 5a). Beyond 90 km, this kernel underestimated the values. A smaller kernel (1500-m azimuthal width)

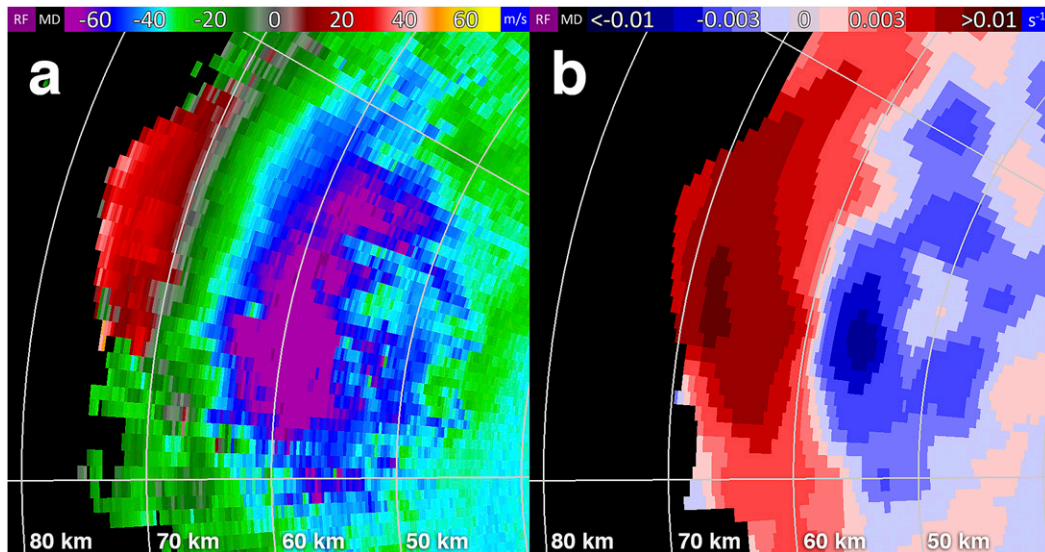


FIG. 8. Single-radar (a) 12.5° dealiased V_r and (b) corresponding DivShear showing a storm-top divergence signature associated with convection from the Oklahoma City, OK (KTLX), radar at 2313 UTC 31 May 2013. The divergence located at the top of the updraft is indicated by strongly positive DivShear and is flanked by a region of negative DivShear in (b). A kernel with an azimuthal width of 750 m and a radial depth of 8750 m was used.

tended to overestimate the rotation intensity of the circulations within 80 km of the radar by 10%–15% while larger kernels resulted in underestimations of 30% (5000-m azimuthal width) to 60% (8000-m azimuthal width) over the same radar distances. These results are caused by small kernels failing to include information from V_r measurements outside of the vortex core and large kernels effectively smoothing the rotation across a larger area. Large kernels are also more sensitive to the physical size of the circulation and produce a wider range of AzShear calculations within 100 km of the radar, as illustrated by the large-area violin plots in

Figs. 4c and 4d and large median-centered interquartile ranges (IQR; Fig. 5b).

Across a diverse set of simulated vortices, the kernel with an azimuthal width of 2500 m and radial depth of 750 m tended to best match theoretical ζ , particularly for those with characteristics common to strong mesocyclones. This kernel size is most appropriate for real-time AzShear calculations given the authors' experience implementing it for severe weather analysis. However, analyses of phenomena of varying scales may find other kernel sizes more appropriate, such as a storm-top divergence signature. In general, larger kernels effectively

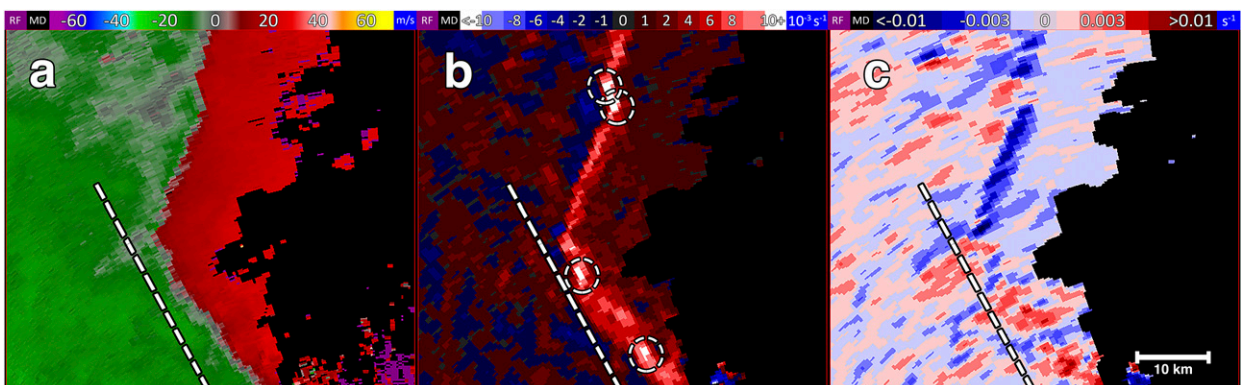


FIG. 9. Single radar, 0.5° (a) dealiased V_r and corresponding (b) AzShear and (c) DivShear associated with a QLCS from the Shreveport, LA (KSHV), radar at 0454 UTC 14 Apr 2018. Strong convergence (blue) occurs along the line in (c) but is not highlighted as such when it is aligned approximately parallel to the KSHV radar beam (approximated by the dashed line). Note several locations of embedded rotation in the AzShear field in (b), denoted by the dashed circles.

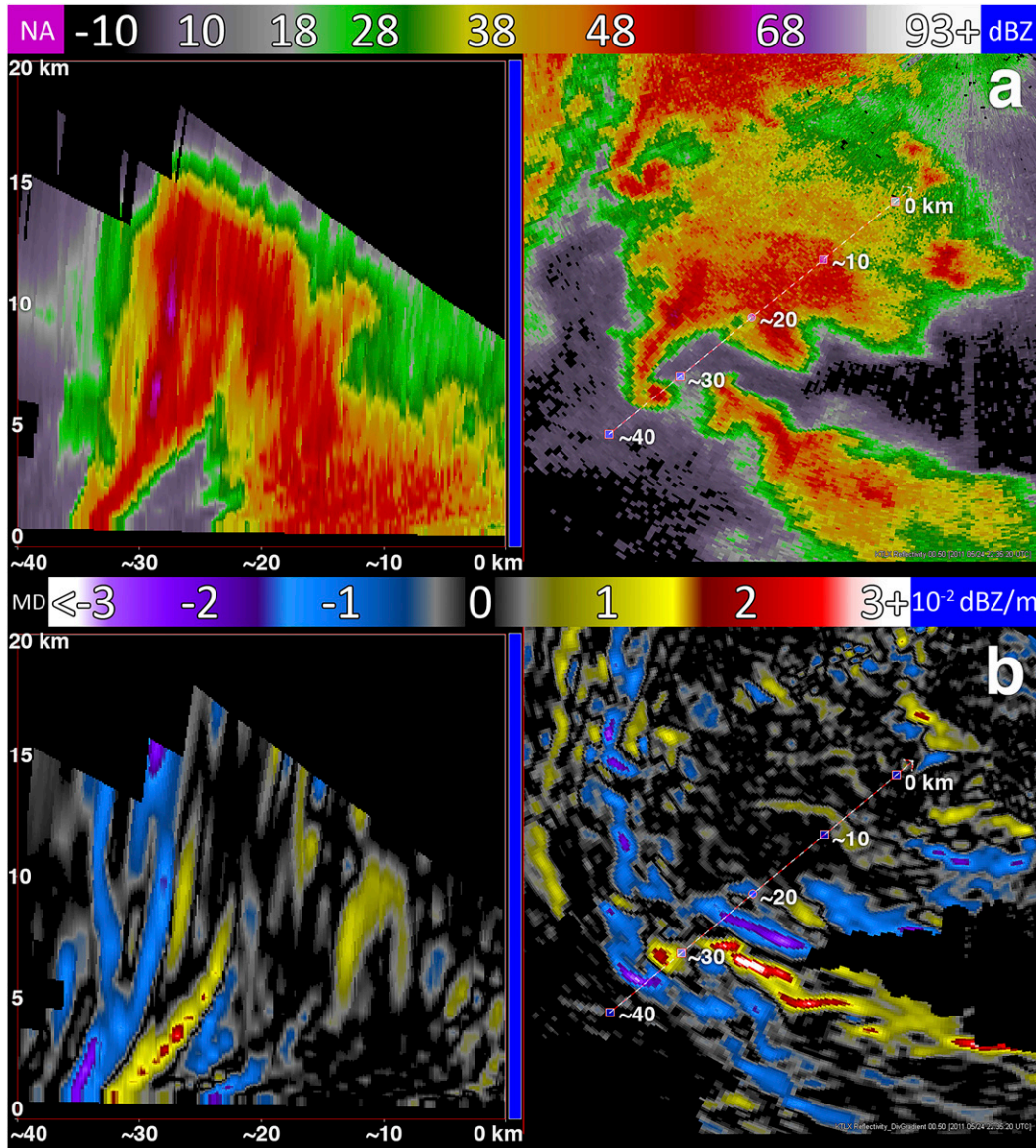


FIG. 10. Single-radar (a) Z_H and (b) corresponding LLS azimuthal Z_H gradient for a tornadic supercell from KTLX at 2235 UTC 24 May 2011. (left) A vertical cross-section taken along the line depicted in the (right) corresponding 0.5° PPI. This multidimensional application of Z_H gradients and the additional context provided by the sign of the gradient can be used to interrogate storm structure.

filter the data more, retaining only the strongest or large-scale gradients. Large-scale derivatives are not removed by smaller kernels, but they may be masked by small-scale gradients that are not resolvable by a larger kernel.

The results shown in Figs. 4–5 are averaged over a representative subset of simulations. A comprehensive analysis of AzShear accuracy relative to small changes in vortex size, strength, and range from radar is beyond the scope of this paper and will be left for future study.

4. Applications

a. Velocity

AzShear and DivShear are the LLSD gradients of V_r fields (Fig. 1) and represent an approximation for half- ζ and half-divergence, respectively. Positive (negative) AzShear values represent cyclonic (anticyclonic) rotation, while positive (negative) DivShear represents divergence (convergence).

Using a different method of calculating AzShear, Burgess et al. (1975) first developed ranges of typical

AzShear values that still largely hold true: AzShear often surpasses $\pm 0.01 \text{ s}^{-1}$ in strong circulations, and the most intense circulations can exceed $\pm 0.05 \text{ s}^{-1}$. Since values tend to be maximized in tornadic supercells (Burgess et al. 1975), AzShear is especially useful for rotation identification and tracking (Manross et al. 2008; Karstens et al. 2016), which, in turn, is valuable for TDS identification (Ryzhkov et al. 2005; Snyder and Ryzhkov 2015) and model verification (Skinner et al. 2016).

The LLSLSD technique has the ability to detect rotation at different spatial scales, with or without changing the kernel size. Data surrounding V_r extrema of any kind will be associated with nonzero AzShear since the extrema are, by definition, greater than the surrounding winds, thus producing a gradient between the two. For example, Fig. 6 shows enhanced AzShear near the strongest winds within the eyewall of a tropical cyclone (Fig. 6b), while also highlighting rotating small-scale features such as tornadic circulations embedded in outer rainbands (Figs. 6d,e), which are often difficult to detect using traditional radar-based algorithms (Spratt et al. 1997).

DivShear was originally used in the development of an experimental damaging downburst detection algorithm (Smith et al. 2004) due to its ability to identify downburst signatures of converging flow aloft and diverging flow near the surface (Fig. 7). It can be also used to identify and investigate supercell structure (Fig. 1; Heinselman et al. 2008) and mesoscale features such as sea breezes and outflow boundaries. Larger-scale divergent features, such as storm-top divergence (Fig. 8), can be examined using LLSLSD kernels with increased radial depth.

Unlike rotation signatures, which are spatially fairly compact and nearly circular, elongated, quasi-linear features like convergence boundaries are a function of radar viewing angle. Along-azimuth gradients are minimized when linear features are oriented parallel to the radar beam, meaning that DivShear values are inherently a function of the feature's orientation to the radar. For example, the quasi-linear convective system (QLCS) depicted in Fig. 9, which produced severe winds and occasional tornadoes, is a line of convergent V_r (Fig. 9a) and an elongated region of AzShear (Fig. 9b). However, the QLCS curves such that its southern half is aligned approximately parallel to the beam, resulting in very little along-azimuth gradient, and locally weak DivShear (Fig. 9c). Given these considerations, some form of the total derivative, or another combination of both shear components, may be useful when examining features with high aspect ratio (e.g., noncircular features such as gust fronts). Interrogating single-radar data from another radar with a different viewing angle of the same feature, or merging data from more than one radar, may also help alleviate this issue.

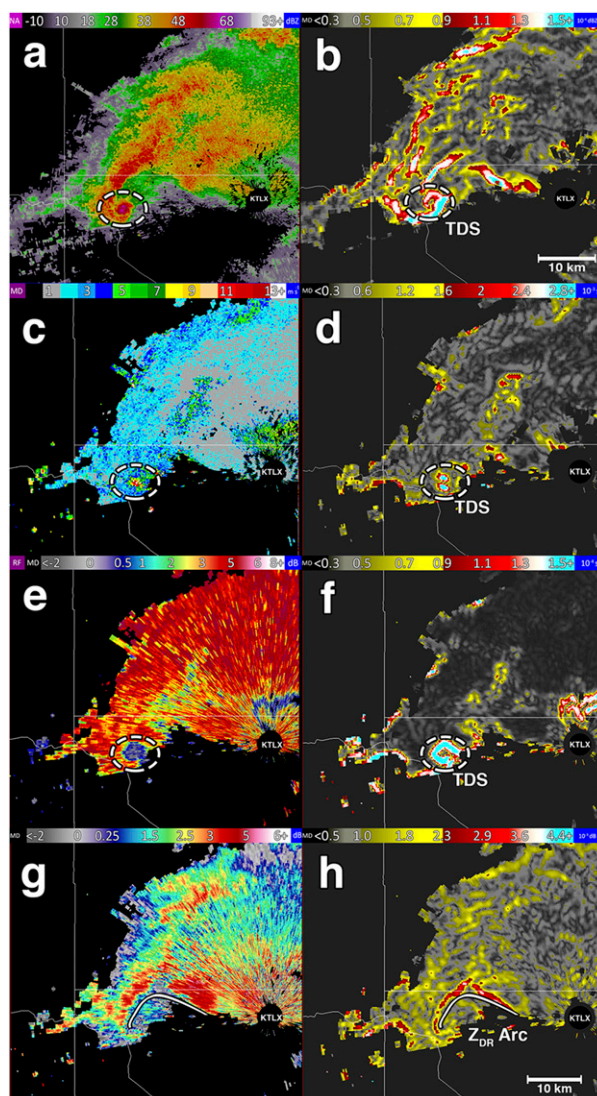


FIG. 11. Single-radar, 0.5° (a) QC Z_H , (c) spectrum width, (e) ρ_{hv} , and (g) Z_{DR} , and (b), (d), (f), (h) corresponding LLSD gradients of each for a tornadic supercell, from KTLX at 2012 UTC 20 May 2013. Polarimetric fields were passed through a preprocessor and thresholded by >20 dBZ QC Z_H . The gradients in (d) and (f) are largest in the vicinity of the tornadic debris signature (denoted by the dashed ellipse) associated with a significant tornado at the time of this scan. The gradient in (h) (denoted by the arched line) highlights a Z_{DR} arc.

Operationally, AzShear is produced within the MRMS system at the National Centers for Environmental Prediction. It is first calculated as a single-radar, layer-maximum product and then is merged onto the MRMS continental United States (CONUS) grid. For example, layer-maximum AzShear is the maximum AzShear within a vertical layer. For the operational MRMS system, two vertical layers are used: low-level [0–2 km above ground level (AGL)] and midlevel

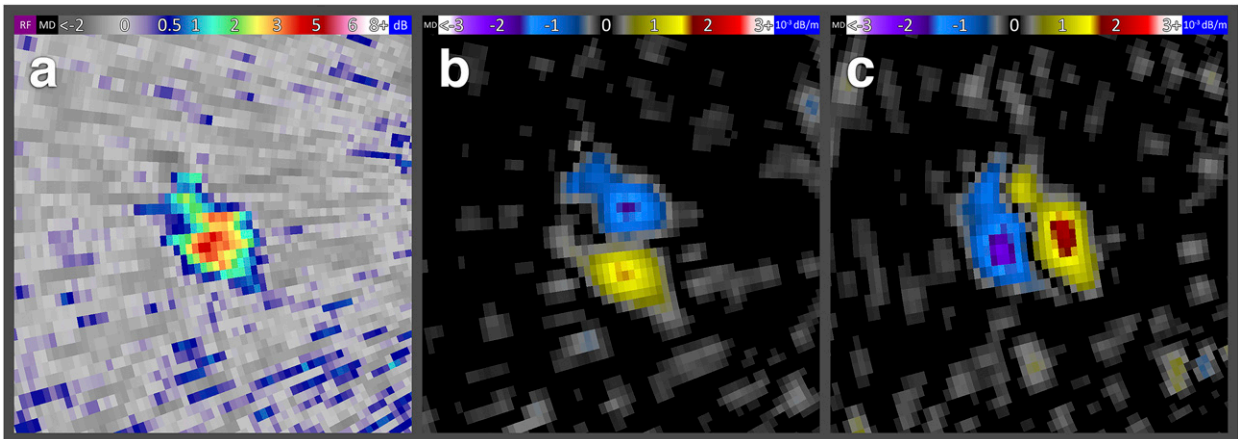


FIG. 12. Single-radar (a) $12.5^\circ Z_{DR}$ and corresponding (b) azimuthal and (c) radial LLS D gradients of a Z_{DR} column within a storm from the Sioux Falls, SD (KFSD), radar at 0352 UTC 18 Jun 2014. Both LLS D gradient components surround the core of a Z_{DR} maximum. Tracking these LLS D gradient peaks over several elevation scans in the same volume can be used to aid in the identification of a Z_{DR} column.

(3–6 km AGL; Smith et al. 2016). Layered AzShear is accumulated over time to produce low- and midlevel rotation tracks (as in Fig. 2), the standard MRMS products used to visualize the paths and intensity trends of mesocyclones (Miller et al. 2013).

b. Reflectivity

For scalar fields, the individual azimuthal and radial LLS D gradients of Z_H and other non- V_r radar fields often provide less meaningful information than V_r gradients but may help reveal features when examined in unison. One method to calculate the total, absolute magnitude of an LLS D gradient is found by calculating the vector norm of the local gradient:

$$\mathbf{u} = \sqrt{u_\theta^2 + u_r^2}. \quad (13)$$

Total Z_H gradients can help identify substorm-scale features such as supercell bounded weak echo regions (BWER) and the vertical structure of precipitation cores (Fig. 10), providing three-dimensional details of Z_H distributions that may help diagnose characteristics of precipitation type, heavy rainfall, hail, or other nonmeteorological scatterers.

The total, horizontal gradient [Eq. (13)] of Z_H (dBZ m^{-1}) effectively produces a Z_H “stencil,” outlining individual storms or Z_H clusters (Figs. 11a,b) by highlighting sharp changes in Z_H , which themselves can be caused by a wide range of meteorological phenomena. For example, a supercell’s shape and the debris ball Z_H signature (a Z_H maximum resulting from lofted debris; Bunkers and Baxter 2011) are seen in the Z_H gradients in Fig. 11b. LLS D Z_H gradient calculations are sensitive to ground clutter contamination, however, and

any nonmeteorological Z_H not removed by quality-control algorithms may interfere with the meteorological signal (Lakshmanan et al. 2007a), as evidenced by isolated, spuriously high LLS D gradient values in Fig. 11 and other nonvelocity gradient figures.

One potential application of LLS D-derived Z_H gradient information could include its implementation within hydrometeor classification or discrimination algorithms. For instance, large hail sizes (diameters exceeding 25 mm) have been observed in low Z_H regions (below 40 dBZ; e.g., Snyder et al. 2014, 2017), while operational algorithms typically use minimum Z_H values at or above 40 dBZ for hail classification and sizing (Witt et al. 1998; Park et al. 2009; Ortega et al. 2016). Use of Z_H gradients instead of or along with simple Z_H thresholds may help improve the skill of these algorithms. The first potential avenue for improvement would be to incorporate the gradient fields into the validation of the algorithms. For instance, Ortega et al. (2016) used only peak reflectivity values at the report point, or within a surrounding neighborhood, to determine the best match for validation. Adding the gradient field might help with more precise matching of reports to algorithm outputs, or at least further stratify results to better explain algorithm skill. The second way would be to directly incorporate gradient fields into the algorithms should they show discrimination power.

c. Spectrum width and polarimetric moments

Gradients of ρ_{hv} (m^{-1}) and spectrum width (s^{-1}) can help indicate the presence of a TDS by highlighting tight gradients surrounding a region of extreme values (Figs. 11c–f; Zrnić and Doviak 1975; Ryzhkov et al. 2005). In some cases, gradients related to important storm properties can visually appear obvious, and thus be useful

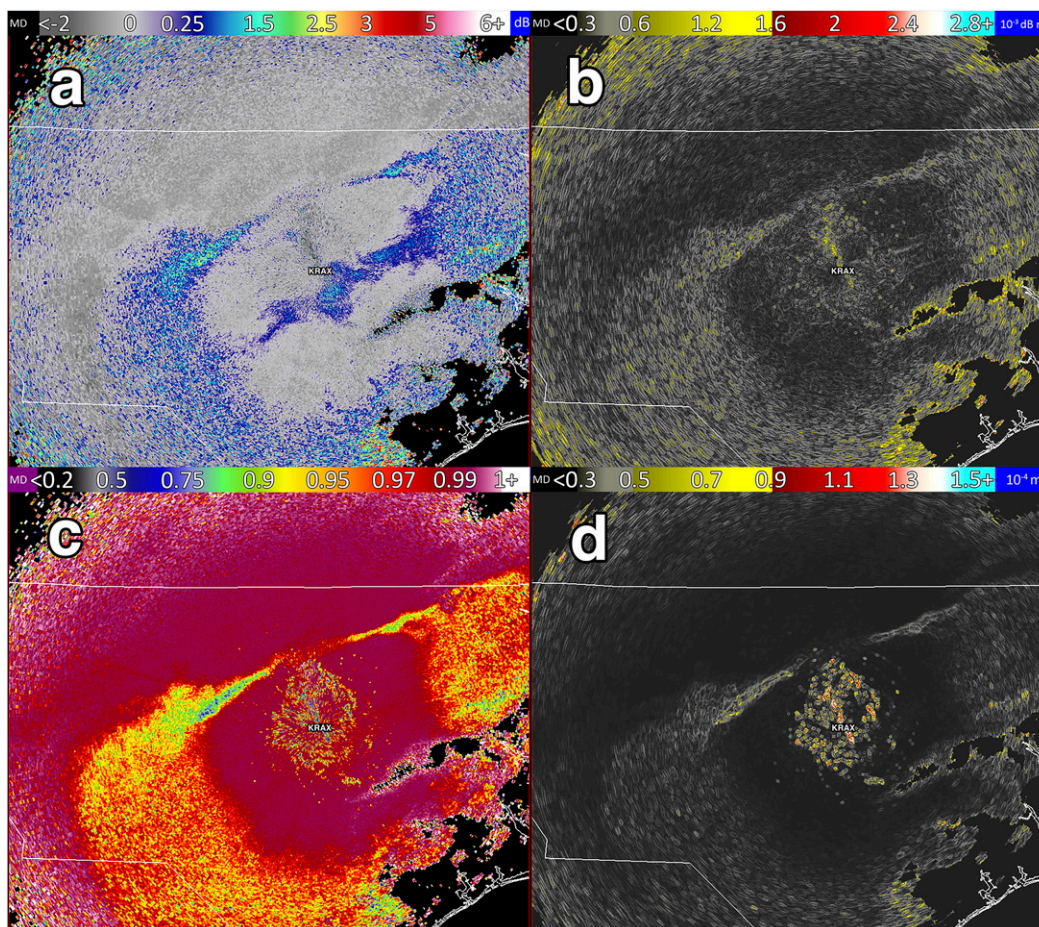


FIG. 13. Single-radar, 0.5°, preprocessed (a) Z_{DR} and (c) ρ_{hv} and (b),(d) corresponding total (i.e., the norm of both components) LLSD gradients of each observed during a winter storm with multiple precipitation types across North Carolina, from the Raleigh/Durham, NC (KRAX), radar at 0310 UTC 7 Jan 2017. Poor ρ_{hv} data quality causes the noisy data near the radar in (c) and (d). In both instances, changes in the relative homogeneity of the gradient fields help distinguish between precipitation types.

during operational applications. At this time, there is no obvious added benefit to using LLSD gradient fields directly in an operational setting, particularly in short-fuse situations, when compared to simply using the human eye. However, these fields reveal patterns in gradients that may be useful in future application development. The examples of polarimetric variable gradients shown here were generated from data processed through the WSR-88D preprocessor (Istok et al. 2009), which smooths the polarimetric variables along the radial and applies corrections to Z_{DR} for attenuation and system calibrations.

In well-organized supercells, Z_{DR} gradients (dB m^{-1}) can highlight Z_{DR} arcs (Figs. 11g,h; Kumjian and Ryzhkov 2008) and Z_{DR} columns (Fig. 12; Kumjian and Ryzhkov 2008), which are related to the magnitude of storm-relative helicity and may diagnose relative updraft strength and hail production, respectively (Kumjian and Ryzhkov 2009). Identifying and monitoring the trends of these

characteristics can help in tracking the location and intensity of individual storms and their hazards.

Gradients of Z_{DR} and ρ_{hv} also show the melting (Ryzhkov et al. 1998) and/or refreezing layers (Kumjian et al. 2013) within both severe convective storms and synoptic-scale winter precipitation (Ryzhkov and Znić 1998) and may help diagnose frozen and mixed-phase cloud physical processes. Values of these products are generally fairly constant across areas of pure snow, while mixed precipitation fields are more heterogeneous due to variations in hydrometeor size and shape. Total LLSD gradients of Z_{DR} and ρ_{hv} detect mixed-phase layers by their heightened spatial variability: many finescale gradients occur within mixed-phase regions, while relatively homogenous precipitation regions contain very few (Fig. 13). Because of the relatively noisy nature of polarimetric data, larger LLSD kernels effectively filter out these signals over a large area.

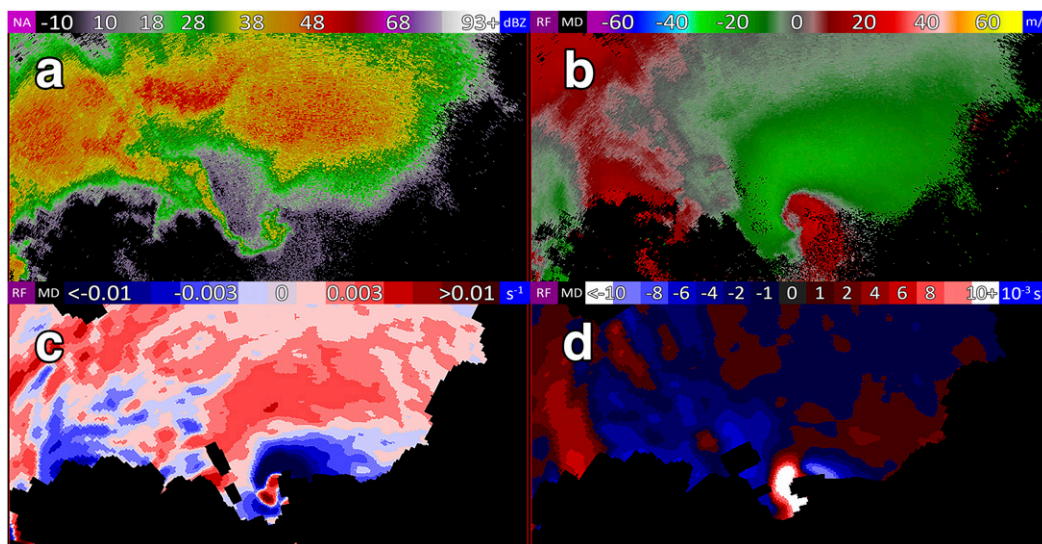


FIG. 14. Single-radar, 0.5° (a) Z_H , (b) dealiased V_r , (c) DivShear, and (d) AzShear from a NOXP sweep of a supercell in western Nebraska at 1659 UTC 13 Jun 2017. Missing DivShear and AzShear in (c) and (d) are caused by missing or range folded data being present in within the LLS D kernel.

Although more analysis is needed to quantify the relationships between non- V_r LLS D gradients and the physical processes described above, it is possible that these gradient calculations, particularly when examined in conjunction with other meteorological data, may aid in ongoing research efforts such as visualizing internal storm processes and isolating regions of particular hydrometeor regimes. Such LLS D gradients may prove especially useful for automated feature detection methods, for example, as input predictors in machine learning applications such as random forest (Breiman 2001) or deep learning (Schmidhuber 2015) classification or identification techniques. Implementation and evaluation of these potential applications will be left to future work. LLS D V_r gradients have already been implemented in the development of new mesocyclone and tornado detection algorithms for the WSR-88D network (Ortega et al. 2018).

d. Radar types

The LLS D algorithms used at NSSL have been optimized to process data from the Weather Surveillance Radar-1988 Doppler (WSR-88D) S-band radars. These radars have changed resolutions over time from legacy (1.38° effective beamwidth; Brown et al. 2002, 2005) to super-resolution (1.02° effective beamwidth; Torres and Curtis 2007) scanning strategies. The algorithm has been successfully tested on both resolutions, though the examples provided in this section apply specifically to super-resolution.

The LLS D equations do not change for data from other, non-WSR-88D systems, such as mobile, C-band, and X-band radars, regardless of spatial or temporal

resolution. The algorithm described here has undergone testing on data from a variety of platforms, including the Rapid-scan X-band Polarimetric mobile radar (RaXPo; Pazmany et al. 2013; Wienhoff et al. 2017) and the NOAA X-band dual-polarized (NOXP; Burgess et al. 2010) mobile radar (Fig. 14), and calculated gradients satisfactorily for each. In addition, LLS D kernel sizes can be manually modified for different radar characteristics, if desired.

e. Data quality

Although the LLS D approach is designed to minimize the effects of poor data quality, it is still subject to the quality of its input field. Operational AzShear blocks out measurements associated with range folding or missing data but will otherwise complete LLS D calculations on the input V_r field. These calculations may be negatively affected by a number of data quality issues, including side-lobe contamination (Piltz and Burgess 2009), dealiasing failures (Figs. 15a,b; Witt et al. 2009), wind farms or other ground clutter (Figs. 15c,d; Isom et al. 2007), and others. For example, in Fig. 15a, artificial AzShear spikes exist along the edges of dealiasing failures, where folds between Nyquist velocity intervals occur. However, since all V_r values elsewhere within the folded region are uniformly affected by the failure, V_r gradients are correct.

5. Summary and future work

An updated derivation and new applications of the improved LLS D approach to calculating gradients in radar data fields have been presented, along with a comprehensive

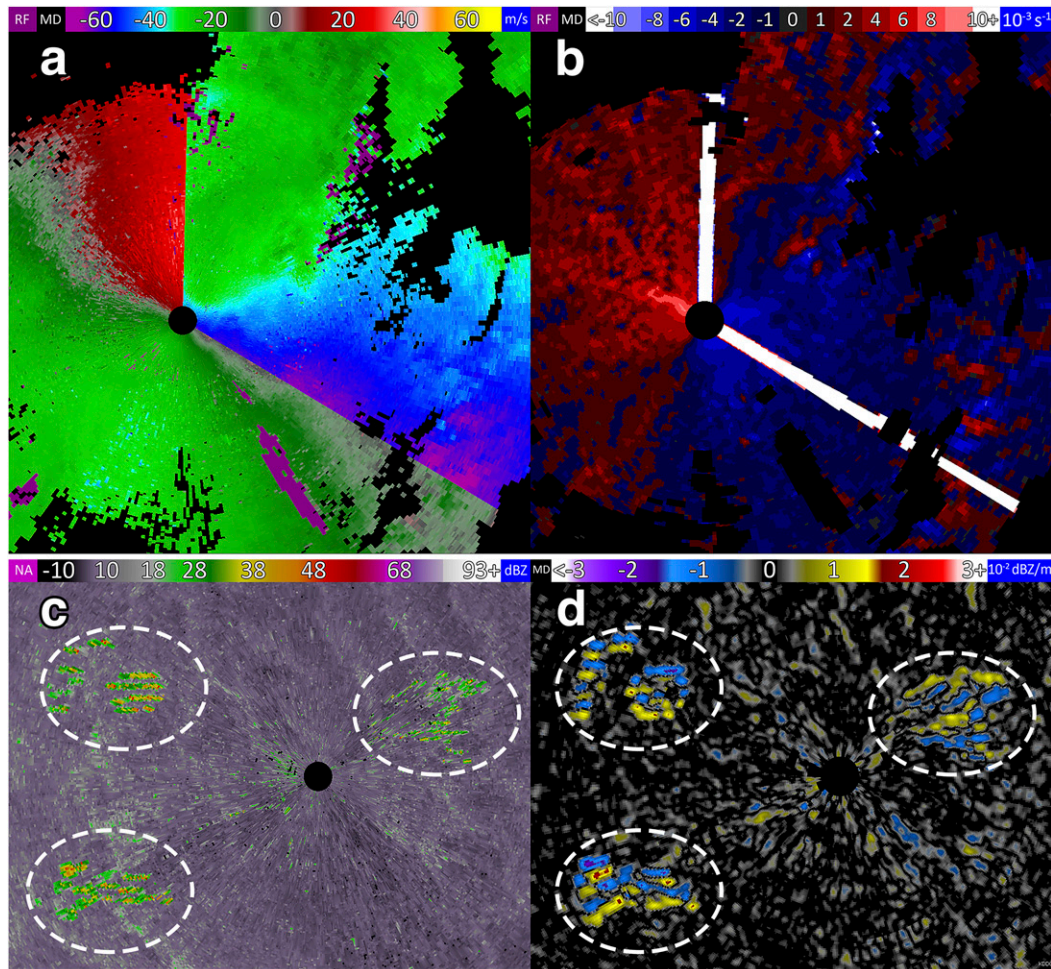


FIG. 15. Examples of poor data quality affecting LLS D gradient calculations. (top) Single-radar (a) 3.1° dealiased V_r and (b) corresponding AzShear from the Kansas City/Pleasant Hill, MO (KEAX), radar at 0221 UTC 20 May 2013. Nonphysical, extreme AzShear occurs along straight lines surrounding a dealiasing failure. (bottom) Single-radar (c) 0.9° Z_H and (d) corresponding LLS D azimuthal Z_H gradient from the Dodge City, KS (KDDC), radar at 2147 UTC 24 May 2016. The Z_H returns are caused by wind farms (denoted by the dashed circles).

discussion of considerations for technique application. The methodology described here can be applied to nearly any radar data field for use in interrogating a wide variety of meteorological phenomena, whether in a manual, user-driven warning-decision sense or perhaps an automated, computer-driven, object-based approach. While up to this point most applications have focused on detecting rotation (AzShear) or aviation hazards (DivShear), LLS D output also may be used as a new approach to depicting storm structure, severe weather signatures, and microphysical processes. However, the work shown here is intended to provide an overview of potential applications, and these analyses represent the minimum that should be done when completing a quantitative analysis of a LLS D product. Use of any LLS D output should be thoroughly tested and evaluated when used in any application.

As with all radar-derived analysis techniques, LLS D products are subject to standard radar sampling limitations. Future work should include thorough documentation of these limitations for specific LLS D applications and an investigation into overcoming them. This may include revisiting previous methods of alleviating range effects (Newman et al. 2013), additional exploration using different kernel sizes for various, feature-specific identifications, and a more expansive investigation of potential kernel weighting techniques.

All LLS D examples in this paper were produced using single-Doppler radar data, but similar multiradar products generated within the MRMS framework should prove useful as well. Thus, the effects of multiradar mergers of LLS D fields, including AzShear, should also be investigated. In addition, further scrutiny of many of

the signatures presented here is necessary, and future work should be performed to test their prevalence.

Acknowledgments. The authors thank Don Burgess for supplying NOXP radar data and assisting in the development of this manuscript. We also thank Vincent Wood and the anonymous reviewers for providing helpful feedback. Funding was provided by NOAA/Office of Oceanic and Atmospheric Research under NOAA–University of Oklahoma Cooperative Agreement NA11OAR4320072, U.S. Department of Commerce.

Additional, partial funding for this work was provided by a Memorandum of Understanding between NSSL and the NEXRAD Program, managed by the Radar Operations Center (ROC).

APPENDIX A

Complete LLSA Azimuthal Gradient Equation

Complete form of the LLSA azimuthal shear (AzShear) equation:

$$\begin{aligned}
 u_{\theta} = & \left(\sum_{k=0}^{m \times n} \Delta r_k^2 \sum_{k=0}^{m \times n} \Delta \theta_k^2 \sum_{k=0}^{m \times n} w_k - \sum_{k=0}^{m \times n} \Delta \theta_k^2 \sum_{k=0}^{m \times n} \Delta r_k \sum_{k=0}^{m \times n} \Delta r_k \right. \\
 & + 2 \sum_{k=0}^{m \times n} \Delta r_k \Delta \theta_k \sum_{k=0}^{m \times n} \Delta r_k \sum_{k=0}^{m \times n} \Delta \theta_k - \sum_{k=0}^{m \times n} \Delta r_k^2 \sum_{k=0}^{m \times n} \Delta \theta_k \sum_{k=0}^{m \times n} \Delta \theta_k \\
 & \left. - \sum_{k=0}^{m \times n} w_k \sum_{k=0}^{m \times n} \Delta r_k \Delta \theta_k \sum_{k=0}^{m \times n} \Delta r_k \Delta \theta_k \right)^{-1} \left[\sum_{k=0}^{m \times n} \Delta r_k u_k \left(\sum_{k=0}^{m \times n} \Delta r_k^2 \sum_{k=0}^{m \times n} w_k \right. \right. \\
 & \left. \left. - \sum_{k=0}^{m \times n} \Delta \theta_k \sum_{k=0}^{m \times n} \Delta \theta_k \right) + \sum_{k=0}^{m \times n} \Delta \theta_k u_k \left(\sum_{k=0}^{m \times n} \Delta r_k \sum_{k=0}^{m \times n} \Delta \theta_k - \sum_{k=0}^{m \times n} \Delta r_k \Delta \theta_k \sum_{k=0}^{m \times n} w_k \right) \right. \\
 & \left. + \sum_{k=0}^{m \times n} u_k \left(\sum_{k=0}^{m \times n} \Delta r_k \Delta \theta_k \sum_{k=0}^{m \times n} \theta_k^2 - \sum_{k=0}^{m \times n} \Delta r_k \sum_{k=0}^{m \times n} \Delta \theta_k^2 \right) \right],
 \end{aligned}$$

where k is the index for each kernel grid point, m and n are the number of grid points in the LLSA kernel in x (m) and y (n), Δr_k is the radial distance from the center of the LLSA kernel, $\Delta \theta_k$ is the azimuthal distance from the center of the LLSA kernel, u_k is the radar variable measurement at kernel grid point k , and w_k is the local weight at kernel grid point k .

APPENDIX B

Complete LLSA Radial Gradient Equation

Complete form of the LLSA radial shear (DivShear) equation:

$$\begin{aligned}
 u_r = & \left(\sum_{k=0}^{m \times n} \Delta r_k^2 \sum_{k=0}^{m \times n} \Delta \theta_k^2 \sum_{k=0}^{m \times n} w_k - \sum_{k=0}^{m \times n} \Delta \theta_k^2 \sum_{k=0}^{m \times n} \Delta r_k \sum_{k=0}^{m \times n} \Delta r_k + 2 \sum_{k=0}^{m \times n} \Delta r_k \Delta \theta_k \sum_{k=0}^{m \times n} \Delta r_k \sum_{k=0}^{m \times n} \Delta \theta_k \right. \\
 & \left. - \sum_{k=0}^{m \times n} \Delta r_k^2 \sum_{k=0}^{m \times n} \Delta \theta_k \sum_{k=0}^{m \times n} \Delta \theta_k \right. \\
 & \left. - \sum_{k=0}^{m \times n} w_k \sum_{k=0}^{m \times n} \Delta r_k \Delta \theta_k \sum_{k=0}^{m \times n} \Delta r_k \Delta \theta_k \right)^{-1} \left[\sum_{k=0}^{m \times n} \Delta r_k u_k \left(\sum_{k=0}^{m \times n} \Delta r_k \sum_{k=0}^{m \times n} \Delta \theta_k \right. \right. \\
 & \left. \left. - \sum_{k=0}^{m \times n} w_k \sum_{k=0}^{m \times n} \Delta r_k \Delta \theta_k \right) + \sum_{k=0}^{m \times n} \Delta \theta_k u_k \left(\sum_{k=0}^{m \times n} \Delta r_k^2 \sum_{k=0}^{m \times n} w_k - \sum_{k=0}^{m \times n} \Delta r_k \sum_{k=0}^{m \times n} \Delta r_k \right) \right. \\
 & \left. + \sum_{k=0}^{m \times n} u_k \left(\sum_{k=0}^{m \times n} \Delta r_k \Delta \theta_k \sum_{k=0}^{m \times n} \Delta r_k - \sum_{k=0}^{m \times n} \Delta \theta_k \sum_{k=0}^{m \times n} \Delta r_k^2 \right) \right],
 \end{aligned}$$

where k is the index for each kernel grid point, m and n are the number of grid points in the LLSA kernel in

x (m) and y (n), Δr_k is the radial distance from the center of the LLSA kernel, $\Delta \theta_k$ is the azimuthal distance from

the center of the LLSD kernel, u_k is the radar variable measurement at kernel grid point k , and w_k is the local weight at kernel grid point k .

REFERENCES

- Alexander, C. R., and J. Wurman, 2008: Updated mobile radar climatology of supercell tornado structures and dynamics. *24th Conf. on Severe Local Storms*, Savannah, GA, Amer. Meteor. Soc., 19.4, <http://ams.confex.com/ams/pdfpapers/141821.pdf>.
- Breiman, L., 2001: Random forests. *Mach. Learn.*, **45**, 5–32, <https://doi.org/10.1023/A:1010933404324>.
- Brown, R. A., L. R. Lemon, and D. W. Burgess, 1978: Tornado detection by pulsed Doppler radar. *Mon. Wea. Rev.*, **106**, 29–38, [https://doi.org/10.1175/1520-0493\(1978\)106<0029:TDBPDR>2.0.CO;2](https://doi.org/10.1175/1520-0493(1978)106<0029:TDBPDR>2.0.CO;2).
- , V. T. Wood, and D. Sirmans, 2002: Improved tornado detection using simulated and actual WSR-88D data with enhanced resolution. *J. Atmos. Oceanic Technol.*, **19**, 1759–1771, [https://doi.org/10.1175/1520-0426\(2002\)019<1759:ITDUSA>2.0.CO;2](https://doi.org/10.1175/1520-0426(2002)019<1759:ITDUSA>2.0.CO;2).
- , B. A. Flickinger, E. Forren, D. M. Schultz, D. Sirmans, P. L. Spencer, V. T. Wood, and C. L. Ziegler, 2005: Improved detection of severe storms using experimental fine-resolution WSR-88D measurements. *Wea. Forecasting*, **20**, 3–14, <https://doi.org/10.1175/WAF832.1>.
- Bunkers, M. J., and M. A. Baxter, 2011: Radar tornadic debris signatures on 27 April 2011. *Electron. J. Oper. Meteor.*, **12**, 1–6.
- Burgess, D. W., L. R. Lemon, and R. A. Brown, 1975: Tornado characteristics revealed by Doppler radar. *Geophys. Res. Lett.*, **2**, 183–184, <https://doi.org/10.1029/GL002i005p00183>.
- , R. J. Donaldson Jr., and P. R. Desrochers, 1993: Tornado detection and warning by radar. *The Tornado: Its Structure, Dynamics, Prediction, and Hazards*, *Geophys. Monogr.*, Vol. 79, Amer. Geophys. Union, 203–221.
- , M. A. Magsig, J. Wurman, D. C. Dowell, and Y. Richardson, 2002: Radar observations of the 3 May 1999 Oklahoma City tornado. *Wea. Forecasting*, **17**, 456–471, [https://doi.org/10.1175/1520-0434\(2002\)017<0456:ROOTMO>2.0.CO;2](https://doi.org/10.1175/1520-0434(2002)017<0456:ROOTMO>2.0.CO;2).
- , E. R. Mansell, C. M. Schwarz, and B. J. Allen, 2010: Tornado and tornadogenesis events seen by the NOXP X-band, dual-polarization radar during VORTEX2 2010. *25th Conf. on Severe Local Storms*, Denver, CO, Amer. Meteor. Soc., 5.2, http://ams.confex.com/ams/25SLS/techprogram/paper_176164.htm.
- , and Coauthors, 2014: 20 May 2013 Moore, Oklahoma, tornado: Damage survey and analysis. *Wea. Forecasting*, **29**, 1229–1237, <https://doi.org/10.1175/WAF-D-14-00039.1>.
- Carbone, R. G., J. W. Conway, N. A. Crook, and M. W. Moncrief, 1990: The generation and propagation of a nocturnal squall line, Part I: Observations and implications for mesoscale predictability. *Mon. Wea. Rev.*, **118**, 26–49, [https://doi.org/10.1175/1520-0493\(1990\)118<0026:TGAPOA>2.0.CO;2](https://doi.org/10.1175/1520-0493(1990)118<0026:TGAPOA>2.0.CO;2).
- Cressman, G. P., 1959: An operational objective analysis system. *Mon. Wea. Rev.*, **87**, 367–374, [https://doi.org/10.1175/1520-0493\(1959\)087<0367:AOOAS>2.0.CO;2](https://doi.org/10.1175/1520-0493(1959)087<0367:AOOAS>2.0.CO;2).
- Davis, J. M., and M. D. Parker, 2014: Radar climatology of tornadic and nontornadic vortices in higher-shear, low-CAPE environments in the mid-Atlantic and southeastern United States. *Wea. Forecasting*, **29**, 828–853, <https://doi.org/10.1175/WAF-D-13-00127.1>.
- Dawson, L. C., G. S. Romine, R. J. Trapp, and M. E. Baldwin, 2017: Verifying supercellular rotation in a convection-permitting ensemble forecasting system with radar-derived rotation track data. *Wea. Forecasting*, **32**, 781–795, <https://doi.org/10.1175/WAF-D-16-0121.1>.
- Donaldson, R. J., Jr., 1970: Vortex signature recognition by a Doppler radar. *J. Appl. Meteor.*, **9**, 661–670, [https://doi.org/10.1175/1520-0450\(1970\)009<0661:VSRBAD>2.0.CO;2](https://doi.org/10.1175/1520-0450(1970)009<0661:VSRBAD>2.0.CO;2).
- , 1978: Observations of the Union City tornadic storm by plan shear indicator. *Mon. Wea. Rev.*, **106**, 39–47, [https://doi.org/10.1175/1520-0493\(1978\)106<0039:OOTUCT>2.0.CO;2](https://doi.org/10.1175/1520-0493(1978)106<0039:OOTUCT>2.0.CO;2).
- Elmore, K. E., E. D. Albo, R. K. Goodrich, and D. J. Peters, 1994: NASA/NCAR airborne and ground-based wind shear studies. Final Rep., Contract NCC1-155, 343 pp.
- Fujita, T. T., 1973: Proposed mechanism of tornado formation from rotating thunderstorms. Preprints, *Eighth Conf. on Severe Local Storms*, Denver, CO, Amer. Meteor. Soc., 191–196.
- Heinselman, P. L., D. L. Priegnitz, K. L. Manross, T. M. Smith, and R. W. Adams, 2008: Rapid sampling of severe storms by the National Weather Radar Testbed Phased Array Radar. *Wea. Forecasting*, **23**, 808–824, <https://doi.org/10.1175/2008WAF2007071.1>.
- , D. S. LaDue, and H. Lazrus, 2012: Exploring impacts of rapid-scan radar data on NWS warning decisions. *Wea. Forecasting*, **27**, 1031–1044, <https://doi.org/10.1175/WAF-D-11-00145.1>.
- Huang, T., G. Yang, and G. Tang, 1979: A fast two-dimensional median filtering algorithm. *IEEE Trans. Acoust. Speech Signal Process.*, **27**, 13–18, <https://doi.org/10.1109/TASSP.1979.1163188>.
- Isom, B. M., and Coauthors, 2007: Characterization and mitigation of wind turbine clutter on the WSR-88D network. *33rd Conf. on Radar Meteorology*, Cairns, Queensland, Australia, Amer. Meteor. Soc., 8B.8, <https://ams.confex.com/ams/33Radar/webprogram/Paper123300.html>.
- Istok, M. J., and Coauthors, 2009: WSR-88D dual polarization initial operating capabilities. *25th Conf. on Int. Interactive Information and Processing Systems (IIPS) for Meteorology, Oceanography, and Hydrology*, Phoenix, AZ, Amer. Meteor. Soc., 15.5, <http://ams.confex.com/ams/pdfpapers/148927.pdf>.
- Karstens, C. D., and Coauthors, 2016: Evaluation of near real-time preliminary tornado damage paths. *J. Oper. Meteor.*, **4**, 132–141, <https://doi.org/10.15191/nwajom.2016.0410>.
- Kumjian, M. R., and A. V. Ryzhkov, 2008: Polarimetric signatures in supercell thunderstorms. *J. Appl. Meteor. Climatol.*, **47**, 1940–1961, <https://doi.org/10.1175/2007JAMC1874.1>.
- , and —, 2009: Storm-relative helicity revealed from polarimetric radar measurements. *J. Atmos. Sci.*, **66**, 667–685, <https://doi.org/10.1175/2008JAS2815.1>.
- , —, H. D. Reeves, and T. J. Schuur, 2013: A dual-polarization radar signature of hydrometeor refreezing in winter storms. *J. Appl. Meteor. Climatol.*, **52**, 2549–2566, <https://doi.org/10.1175/JAMC-D-12-0311.1>.
- Kuster, C. M., P. L. Heinselman, J. C. Snyder, K. A. Wilson, D. A. Speheger, and J. E. Hocker, 2017: An evaluation of radar-based tornado track estimation products by Oklahoma public safety officials. *Wea. Forecasting*, **32**, 1711–1726, <https://doi.org/10.1175/WAF-D-17-0031.1>.
- Lakshmanan, V., A. Fritz, T. Smith, K. Hondl, and G. Stumpf, 2007a: An automated technique to quality control radar reflectivity data. *J. Appl. Meteor. Climatol.*, **46**, 288–305, <https://doi.org/10.1175/JAM2460.1>.
- , T. Smith, G. J. Stumpf, and K. Hondl, 2007b: The Warning Decision Support System-Integrated Information. *Wea. Forecasting*, **22**, 596–612, <https://doi.org/10.1175/WAF1009.1>.

- Manross, K. L., T. M. Smith, J. T. Ferree, and G. J. Stumpf, 2008: An on-demand user interface for requesting multi-radar, multi-sensor time accumulated products to support severe weather verification. *24th Conf. on Interactive Information Processing Systems*, New Orleans, LA, Amer. Meteor. Soc., P2.13, https://ams.confex.com/ams/88Annual/techprogram/paper_134621.htm.
- Markowski, P. M., 2002: Hook echoes and rear-flank downdrafts: A review. *Mon. Wea. Rev.*, **130**, 852–876, [https://doi.org/10.1175/1520-0493\(2002\)130<0852:HEARFD>2.0.CO;2](https://doi.org/10.1175/1520-0493(2002)130<0852:HEARFD>2.0.CO;2).
- Miller, M. L., V. Lakshmanan, and T. M. Smith, 2013: An automated method for depicting mesocyclone paths and intensities. *Wea. Forecasting*, **28**, 570–585, <https://doi.org/10.1175/WAF-D-12-00065.1>.
- Mitchell, E. D., S. V. Vasiloff, G. J. Stumpf, A. Witt, M. D. Eilts, J. T. Johnson, and K. W. Thomas, 1998: The National Severe Storms Laboratory tornado detection algorithm. *Wea. Forecasting*, **13**, 352–366, [https://doi.org/10.1175/1520-0434\(1998\)013<0352:TNSSLT>2.0.CO;2](https://doi.org/10.1175/1520-0434(1998)013<0352:TNSSLT>2.0.CO;2).
- Newman, J. F., V. Lakshmanan, P. L. Heinselman, M. B. Richman, and T. M. Smith, 2013: Range-correcting azimuthal shear in Doppler radar data. *Wea. Forecasting*, **28**, 194–211, <https://doi.org/10.1175/WAF-D-11-00154.1>.
- Ortega, K. L., J. M. Krause, and A. V. Ryzhkov, 2016: Polarimetric radar characteristics of melting hail. Part III: Validation of the algorithm for hail size discrimination. *J. Appl. Meteor. Climatol.*, **55**, 829–848, <https://doi.org/10.1175/JAMC-D-15-0203.1>.
- , D. W. Burgess, K. L. Elmore, M. C. Mahalik, and B. R. Smith, 2018: Severe weather algorithm development and improvement activities for the WSR-88D at NSSL/CIMMS under the ROC tech transfer MOU. *29th Conf. on Weather Analysis and Forecasting*, Denver, CO, Amer. Meteor. Soc., 12A.4, <https://ams.confex.com/ams/29WAF25NWP/webprogram/Paper344948.html>.
- Park, H.-S., A. V. Ryzhkov, D. S. Zrnić, and K.-E. Kim, 2009: The hydrometeor classification algorithm for the polarimetric WSR-88D: Description and application to an MCS. *Wea. Forecasting*, **24**, 730–748, <https://doi.org/10.1175/2008WAF2222205.1>.
- Pazmany, A. L., J. B. Mead, H. B. Bluestein, J. C. Snyder, and J. B. Houser, 2013: A mobile, rapid-scanning, X-band, polarimetric (RaXPo) Doppler radar system. *J. Atmos. Oceanic Technol.*, **30**, 1398–1413, <https://doi.org/10.1175/JTECH-D-12-00166.1>.
- Piltz, S. F., and D. W. Burgess, 2009: The impacts of thunderstorm geometry and WSR-88D beam characteristics on diagnosing supercell tornadoes. *34th Conf. on Radar Meteorology*, Williamsburg, VA, Amer. Meteor. Soc., P6.18, https://ams.confex.com/ams/34Radar/techprogram/paper_155944.htm.
- Przybylinski, R. W., 1995: The bow echo: Observations, numerical simulations, and severe weather detections. *Wea. Forecasting*, **10**, 203–218, [https://doi.org/10.1175/1520-0434\(1995\)010<0203:TBEONS>2.0.CO;2](https://doi.org/10.1175/1520-0434(1995)010<0203:TBEONS>2.0.CO;2).
- Roberts, R. D., and J. W. Wilson, 1989: A proposed microburst nowcasting procedure using single-Doppler radar. *J. Appl. Meteor. Climatol.*, **28**, 285–303, [https://doi.org/10.1175/1520-0450\(1989\)028<0285:APMNPV>2.0.CO;2](https://doi.org/10.1175/1520-0450(1989)028<0285:APMNPV>2.0.CO;2).
- Ryzhkov, A. V., and D. S. Zrnić, 1998: Discrimination between rain and snow with a polarimetric radar. *J. Appl. Meteor.*, **37**, 1228–1240, [https://doi.org/10.1175/1520-0450\(1998\)037<1228:DBRASW>2.0.CO;2](https://doi.org/10.1175/1520-0450(1998)037<1228:DBRASW>2.0.CO;2).
- , —, and B. A. Gordon, 1998: Polarimetric method for ice water content determination. *J. Appl. Meteor.*, **37**, 125–134, [https://doi.org/10.1175/1520-0450\(1998\)037<0125:PMFIWC>2.0.CO;2](https://doi.org/10.1175/1520-0450(1998)037<0125:PMFIWC>2.0.CO;2).
- , T. J. Schuur, D. W. Burgess, and D. S. Zrnić, 2005: Polarimetric tornado detection. *J. Appl. Meteor. Climatol.*, **44**, 557–570, <https://doi.org/10.1175/JAM2235.1>.
- Schmidhuber, J., 2015: Deep learning in neural networks: An overview. *Neural Networks*, **61**, 85–117, <https://doi.org/10.1016/j.neunet.2014.09.003>.
- Schmocker, G. K., R. W. Przybylinski, and Y. J. Lin, 1996: Forecasting the initial onset of damaging downburst winds associated with a Mesoscale Convective System (MCS) using the Mid-Altitude Radial Convergence (MARC) signature. Preprints, *15th Conf. on Weather Analysis and Forecasting*, Norfolk, VA, Amer. Meteor. Soc., 306–311.
- Skinner, P. S., L. J. Wicker, D. M. Wheatley, and K. H. Knopfmeier, 2016: Application of two spatial verification methods to ensemble forecasts of low-level rotation. *Wea. Forecasting*, **31**, 713–735, <https://doi.org/10.1175/WAF-D-15-0129.1>.
- Smith, B. T., R. L. Thompson, A. R. Dean, and P. T. Marsh, 2015: Diagnosing the conditional probability of tornado damage rating using environmental and radar attributes. *Wea. Forecasting*, **30**, 914–932, <https://doi.org/10.1175/WAF-D-14-00122.1>.
- Smith, T. M., and K. L. Elmore, 2004: The use of radial velocity derivatives to diagnose rotation and divergence. Preprints, *11th Conf. on Aviation, Range, and Aerospace*, Hyannis, MA, Amer. Meteor. Soc., P5.6, <http://ams.confex.com/ams/pdfpapers/81827.pdf>.
- , —, and S. A. Dulin, 2004: A damaging downburst prediction and detection algorithm for the WSR-88D. *Wea. Forecasting*, **19**, 240–250, [https://doi.org/10.1175/1520-0434\(2004\)019<0240:ADDPAD>2.0.CO;2](https://doi.org/10.1175/1520-0434(2004)019<0240:ADDPAD>2.0.CO;2).
- , and Coauthors, 2016: Multi-Radar Multi-Sensor (MRMS) severe weather and aviation products: Initial operating capabilities. *Bull. Amer. Meteor. Soc.*, **97**, 1617–1630, <https://doi.org/10.1175/BAMS-D-14-00173.1>.
- Snyder, J. C., and A. V. Ryzhkov, 2015: Automated detection of polarimetric tornadic debris signatures using a hydrometeor classification algorithm. *J. Appl. Meteor. Climatol.*, **54**, 1861–1870, <https://doi.org/10.1175/JAMC-D-15-0138.1>.
- , —, H. B. Bluestein, and S. F. Blair, 2014: Polarimetric analysis of two giant-hail producing supercells by X-band and S-band radars. *27th Conf. on Severe Local Storms*, Madison, WI, Amer. Meteor. Soc., 166, <https://ams.confex.com/ams/27SLS/webprogram/Paper255455.html>.
- , —, J. Krause, and C. Kuster, 2017: Identifying polarimetric radar signatures aloft associated with large and giant hail. *38th Conf. on Radar Meteorology*, Chicago, IL, Amer. Meteor. Soc., 237, <https://ams.confex.com/ams/38RADAR/meetingapp/cgi/Paper321184>.
- Spratt, S. M., D. W. Sharp, P. Welsh, A. Sandrik, F. Alsheimer, and C. Paxton, 1997: A WSR-88D assessment of tropical cyclone outer rainband tornadoes. *Wea. Forecasting*, **12**, 479–501, [https://doi.org/10.1175/1520-0434\(1997\)012<0479:AWAOTC>2.0.CO;2](https://doi.org/10.1175/1520-0434(1997)012<0479:AWAOTC>2.0.CO;2).
- Stough, S. M., L. D. Carey, C. J. Schultz, and P. M. Bitzer, 2017: Investigating the relationship between lightning and mesocyclonic rotation in supercell thunderstorms. *Wea. Forecasting*, **32**, 2237–2259, <https://doi.org/10.1175/WAF-D-17-0025.1>.
- Stumpf, G. J., A. Witt, E. D. Mitchell, P. L. Spencer, J. T. Johnson, M. D. Eilts, K. W. Thomas, and D. W. Burgess, 1998: The National Severe Storms Laboratory mesocyclone detection algorithm for the WSR-88D. *Wea. Forecasting*, **13**, 304–326, [https://doi.org/10.1175/1520-0434\(1998\)013<0304:TNSSLM>2.0.CO;2](https://doi.org/10.1175/1520-0434(1998)013<0304:TNSSLM>2.0.CO;2).

- , and Coauthors, 2012: The Experimental Warning Program's 2011 and 2012 Spring Experiments at the NOAA Hazardous Weather Testbed. *26th Conf. on Severe Local Storms*, Nashville, TN, Amer. Meteor. Soc., 3.4, <https://ams.confex.com/ams/26SLS/webprogram/Paper212324.html>.
- Thompson, R. L., and Coauthors, 2017: Tornado damage rating probabilities derived from WSR-88D data. *Wea. Forecasting*, **32**, 1509–1528, <https://doi.org/10.1175/WAF-D-17-0004.1>.
- Torres, S. M., and C. D. Curtis, 2007: Initial implementation of super-resolution data on the NEXRAD network. *23rd Conf. on Information Processing Systems*, San Antonio, TX, Amer. Meteor. Soc., 5B.10, https://ams.confex.com/ams/87ANNUAL/techprogram/paper_116240.htm.
- Wienhoff, Z. B., H. B. Bluestein, L. J. Wicker, J. C. Snyder, A. Shapiro, C. K. Potvin, and D. W. Reif, 2017: An analysis of the evolution and structure of a multiple-tornado-producing supercell near Dodge City, KS, on 24 May 2016. *38th Conf. on Radar Meteorology*, Chicago, IL, Amer. Meteor. Soc., 147, <https://ams.confex.com/ams/38RADAR/meetingapp.cgi/Paper/320832>.
- Wilson, J. W., G. B. Foote, N. A. Crook, J. C. Fankhouser, C. G. Wade, J. D. Tuttle, C. K. Mueller, and S. K. Krueger, 1992: The role of boundary-layer convergence zones and horizontal rolls in the initiation of thunderstorms: A case study. *Mon. Wea. Rev.*, **120**, 1785–1815, [https://doi.org/10.1175/1520-0493\(1992\)120<1785:TROBLC>2.0.CO;2](https://doi.org/10.1175/1520-0493(1992)120<1785:TROBLC>2.0.CO;2).
- Witt, A., M. D. Eilts, G. J. Stumpf, J. T. Johnson, E. D. Mitchell, and K. W. Thomas, 1998: An enhanced hail detection algorithm for the WSR-88D. *Wea. Forecasting*, **13**, 286–303, [https://doi.org/10.1175/1520-0434\(1998\)013<0286:AEHDAF>2.0.CO;2](https://doi.org/10.1175/1520-0434(1998)013<0286:AEHDAF>2.0.CO;2).
- , R. A. Brown, and Z. Jing, 2009: Performance of a new velocity dealiasing algorithm for the WSR-88D. *34th Conf. on Radar Meteorology*, Williamsburg, VA, Amer. Meteor. Soc., P4.8, https://ams.confex.com/ams/34Radar/techprogram/paper_155951.htm.
- Wood, V. T., and R. A. Brown, 1997: Effects of radar sampling on single-Doppler velocity signatures of mesocyclones and tornadoes. *Wea. Forecasting*, **12**, 928–938, [https://doi.org/10.1175/1520-0434\(1997\)012<0928:EORSOS>2.0.CO;2](https://doi.org/10.1175/1520-0434(1997)012<0928:EORSOS>2.0.CO;2).
- , and —, 2011: Simulate tornadic vortex signatures of tornado-like vortices having one- and two-celled structures. *J. Appl. Meteor. Climatol.*, **50**, 2338–2342, <https://doi.org/10.1175/JAMC-D-11-0118.1>.
- Zittel, W. D., R. R. Lee, E. D. Mitchell, and D. Sirmans, 2001: Environmental and signal processing conditions that negatively impact the performance of the WSR-88D tornado detection algorithm. *30th Int. Conf. on Radar*, Munich Germany, Amer. Meteor. Soc., 12B.6, <https://ams.confex.com/ams/pdfpapers/19862.pdf>.
- Zrnčić, D. S., and R. J. Doviak, 1975: Velocity spectra of vortices scanned with a pulse-Doppler radar. *J. Appl. Meteor.*, **14**, 1531–1539, [https://doi.org/10.1175/1520-0450\(1975\)014<1531:VSOVSW>2.0.CO;2](https://doi.org/10.1175/1520-0450(1975)014<1531:VSOVSW>2.0.CO;2).